LAWRENCE
LIVERMORE
NATIONAL
LABORATORY

A coupled thermo-hydro-mechanical model for simulating leakoff-dominated hydraulic fracturing with application to geologic carbon storage

X. Ju, P. Fu, R. Settegast, J. Morris

November 16, 2020

Disclaimer

This document was prepared as an account of work sponsored by an agency of the United States government. Neither the United States government nor Lawrence Livermore National Security, LLC, nor any of their employees makes any warranty, expressed or implied, or assumes any legal liability or responsibility for the accuracy, completeness, or usefulness of any information, apparatus, product, or process disclosed, or represents that its use would not infringe privately owned rights. Reference herein to any specific commercial product, process, or service by trade name, trademark, manufacturer, or otherwise does not necessarily constitute or imply its endorsement, recommendation, or favoring by the United States government or Lawrence Livermore National Security, LLC. The views and opinions of authors expressed herein do not necessarily state or reflect those of the United States government or Lawrence Livermore National Security, LLC, and shall not be used for advertising or product endorsement purposes.

1   **A coupled thermo-hydro-mechanical model for simulating leakoff-dominated hydraulic**

2   **fracturing with application to geologic carbon storage**

3

4   Xin Ju, Pengcheng Fu*, Randolph Settegast, Joseph Morris

5

6   Atmospheric, Earth, and Energy Division, Lawrence Livermore National Laboratory, Livermore,

7   CA 94550 USA.

8

9   *Corresponding author: fu4@llnl.gov

10

11   Abstract: A potential risk of injecting CO_2 into storage reservoirs with marginal permeability

12   ($\lesssim$ 10 mD (1 mD = 10^{-15} m^2)) is that commercial injection rates could induce fracturing of the

13   reservoir and/or the caprock. Such fracturing is essentially fluid-driven fracturing in the leakoff-

14   dominated regime. Recent studies suggested that fracturing, if contained within the lower portion

15   of the caprock complex, could substantially improve the injectivity without compromising the

16   overall seal integrity. Modeling this phenomenon entails complex coupled interactions among the

17   fluids, the fracture, the reservoir, and the caprock. We develop a simple method to capture all

18   these interplays in high fidelity by sequentially coupling a hydraulic fracturing module with a

19   coupled thermal-hydrological-mechanical (THM) model for nonisothermal multiphase flow. The

20   model was made numerically tractable by taking advantage of self-stabilizing features of leakoff-

21   dominated fracturing. The model is validated against the PKN solution in the leakoff-dominated

22   regime. Moreover, we employ the model to study thermo-poromechanical responses of a fluid-

23   driven fracture in a field-scale carbon storage reservoir that is loosely based on the In Salah

24   project's Krechba reservoir. The model reveals complex yet intriguing behaviors of the

25   reservoir-caprock-fluid system with fracturing induced by cold CO_2 injection. We also study the

26   effects of the *in situ* stress contrast between the reservoir and caprock and thermal contraction on

27   the vertical containment of the fracture. The proposed model proves effective in simulating

28   practical problems on length and time scales relevant to geological carbon storage.

29

30   Keywords: Geologic carbon storage, CO_2 fracturing, THM coupled modeling, multiphase

31   multicomponent fluid flow, supercritical CO_2

32   **1   Introduction**

33

34   Geological carbon storage (GCS) is a promising measure to mitigate the effect of anthropogenic

35   greenhouse gas emissions on climate change (Pacala and Socolow, 2004; International Energy

36   Agency, 2010). To have a meaningful impact on the net CO_2 emission through GCS requires

37   injecting a large quantity of CO_2 into subsurface geological reservoirs (Orr, 2009; Haszeldine,

38   2009). Existing pilot and experimental GCS projects mainly focus on storage reservoirs with

39   ideal conditions, such as high porosity and high permeability (typically in the range of hundreds

40   to thousands of millidarcy (1 mD $= 10^{-15}$ m^2)). Considering that high quality reservoirs do not

41   necessarily exist near CO_2 sources, the utilization of less favorable reservoirs, such as those with

42   marginal permeabilities (i.e. low tens of mD), can significantly improve the commercial viability

43   of GCS. In particular, recent commercial-scale field tests demonstrate that many such low

44   permeability reservoirs have enormous CO_2 sources nearby and also enjoy easy access to drilling

45   and comprehensive monitoring systems (Mito et al., 2008, Rinaldi et al, 2013). One good

46   example of such sites is In Salah, Algeria, where a large amount of CO_2 source from nearby

47   natural gas production was injected into several storage reservoirs with marginal permeabilities

48   (around 10 mD) (Iding and Ringrose, 2010; Rinaldi et al., 2013). Therefore, understanding GCS

49   in reservoirs with marginal permeability is of great significance.

50   The main challenge facing injection into marginal-permeability reservoirs is the low injectivity

51   under the pressure constraints that prevent fluid-driven fractures, namely, hydraulic fractures,

52   from occurring in storage reservoirs. Previous studies showed that using a low injection rate that

53   complies with the pressure constraint cannot achieve even a moderate commercial-level injection

54   rate, i.e. a million-metric ton per year per well (Fu et al., 2017). However, recent studies

55   postulated that the issue of low injectivity in marginal-permeability reservoirs might be

56   effectively and safely mitigated if injection-triggered hydraulic fractures can be contained within

57   reservoir rocks or the lower portion of the caprock without jeopardizing the overall seal integrity

58   of the caprock complex (White et al., 2014; Fu et al., 2017). Circumstantial field data and

59   observations from the In Salah site also suggest the possible existence of such postulated

60   scenarios (Bohloli et al., 2017; Oye et al., 2013; White et al., 2014).

61   Modeling hydraulic fracturing in marginal-permeability GCS reservoirs entails the simulation of

62   many complex processes: multiphase multicomponent fluid flow and heat transfer within

63   fractures and matrix, mass and heat exchanges between fracture and matrix flows, poro/thermo-

64   elastic deformation of solid rocks, and fracture propagation. Although many numerical studies

65   have tackled this challenging task, significant simplifications had been made to mitigate various

66   numerical challenges. These simplifications could be broadly divided into two groups: (1)

67   treating hydraulic fractures as a highly permeable porous zone and (2) simplifying multiphase

68   and nonisothermal flow behaviors of injected CO_2.

69   The first group of works typically simplify the dynamic interactions between fracture

70   propagation and matrix flows and also neglect some key characteristics of hydraulic fractures

71   (e.g. Morris et al., 2011; Pan et al., 2012; Raziperchikolaee et al., 2013; Sun et al., 2016). In

72   other words, these are not designed to accurately predict the coupled thermo-hydro-mechanical

73   (THM) responses of reservoir and caprocks once fluid-driven fractures are created. Many models

74   in this category employ a continuum-based method, such as the dual porosity models and dual

75   permeability models (e.g. Guo et al., 2017; Li and Elsworth 2019; Fan et al., 2019), neither of

76   which could represent the complex flow behaviors associated with a propagating fracture.

77   Moreover, works that attempt to capture geomechanical responses of hydraulic fractures often do

78   not address complexities caused by an evolving fracture tip (e.g. Gor et al. 2014; Eshiet and

79   Sheng 2014; Vilarrasa et al., 2014). In other words, they cannot explicitly depict the evolution of

80   fracture extents and shapes which is critical to evaluating fracture containment (Rutqvist et al.,

81   2016; Ren et al., 2017; Vilarrasa et al., 2017; Sun et al., 2017).

82   The second group of works, on the other hand, strive to capture essential features associated with

83   hydraulic fracturing, such as fracturing propagation, seepage (leakoff) of fluid through fractures

84   into reservoirs, and strong nonlinearity of the coupling between fracture permeability and

85   hydraulic aperture (Fu et al., 2017; Culp et al., 2017; Salimzadeh et al., 2017; Salimzadeh et al.,

86   2018; Gheibi et al. 2018; Mollaali et al., 2019; Yan et al., 2020), but substantially simplify fluid

87   flow characteristics unique to supercritical CO_2 flow in a saline reservoir. The works of Fu et al.

88   (2017) and Yan et al. (2020) focused on modeling isothermal fluid flow in porous media and

89   ignored the thermal responses of fractures in the storage reservoir. However, these responses

90   have a great impact on caprock integrity (Vilarrasa et al., 2014; Kim and Hosseini, 2014; Kim

91   and Hosseini, 2015; Salimzadeh et al., 2018). The simulations conducted by Salimzadeh et al.

92 (2018) used a surrogate flow model—single-phase flow model— for simulating two-phase CO_2

93 flow, neglecting the pressure- and temperature- dependency of the PVT (pressure, volume,

94 temperature) properties and multiphase flow of supercritical CO_2. In addition to discrete fracture

95 models used by the above studies, smeared fracture models, such as the phase field method

96 (Francfort and Marigo, 1998; Francfort et al., 2008), have also been adapted to address hydraulic

97 fracturing related to CO_2 injection. Although it is straightforward to integrate the mass and

98 energy conservations of CO_2 into the general formulation of the phase field method and to

99 consider complex fracture processes (e.g. Culp et al., 2017; Mollaali et al., 2019), the smearing

100 nature of this approach, nonetheless, poses stringent requirements on mesh refinement and

101 adaptivity to accurately reconstruct the displacement discontinuities across the fracture surface

102 (Lecampion et al., 2017). This numerical challenge has limited the application of the phase field

103 to small-scale simulations (Mollaali et al., 2019). According to the latest review on the modeling

104 of caprock integrity (Paluszny et al. 2020), a fully coupled 3D model that can capture the

105 complex interplay among CO_2 injection, reservoir responses, and the propagation of hydraulic

106 fractures at the field-scale is not currently available. The scarcity of such models is likely owing

107 to the lack of a modeling scheme that can effectively and efficiently simulate the inherent

108 complexity of hydraulic fracturing in marginal-permeability GCS reservoirs.

109 The objective of this study is to develop a modeling scheme that effectively and efficiently

110 simulates hydraulic fracturing in GCS reservoirs and to study the mechanisms of fracture

111 containment within the caprock formations. The proposed scheme is particularly designed to

112 simulate the interactions between coupled THM processes in a CO_2 storage system (reservoir

113 and caprock) and the propagation of a fluid-driven fracture in the so-called "leakoff-dominated"

114 regime (Bunger et al., 2005; Detournay, 2016). As revealed by Fu et al. (2017), hydraulic

115   fracture propagation driven by CO_2 injection into a storage reservoir is expected to be in this

116   regime, in which the majority of the injected fluid leaks from the hydraulic fracture and is stored

117   in the storage reservoir. The propagation rate of the fracture is dominated by the leakoff rate into

118   the reservoir. Mechanical responses of the fracture do not strongly affect the propagation rate, in

119   sharp contrast to fracture behavior in the so-called storage-dominated and toughness-dominated

120   regimes. This particular feature enables us to couple hydraulic fracturing and the associated rock

121   deformation with reservoir flow in a simple yet sufficiently accurate way.

122   This paper proceeds as follows. Section 2 describes the mathematical formulations of a coupled

123   THM model and the proposed modeling scheme that couples the THM model with a fracture

124   mechanics module. The underlying rationale of this scheme is also discussed in this section.

125   Section 3 validates the proposed scheme by comparing numerical results against the PKN

126   solution in the leakoff-dominated regime. In Section 4 we build a 3D field-scale model, loosely

127   based on the In Salah Project and reveal complex interplays between hydraulic fracturing and

128   thermo-poroelastic effects induced by cold CO_2 injection. Section 5 discusses the effects of

129   various reservoir conditions in the context of GCS, on the controlling mechanisms of the growth

130   of caprock fracture. In the concluding section, we suggest possible implications of the proposed

131   method and findings for GCS site characterization and operation.

132   **2   Methodology**

133   In this section, we briefly describe the governing equations of the coupled THM processes taking

134   discrete hydraulic fractures into account. Next, we introduce the coupling scheme that links the

135   coupled THM model to a fracture mechanics module in a simple yet accurate fashion. Note that

136   the THM model used here is an extension of the continuum based THM model as described in

137   Fu et al. (2020). More details related to that THM model, such as derivation of governing

138 equations of multiphase multicomponent flow and heat transfer, numerical discretization, and

139 fixed-stress iterative scheme, can be found in Fu et al. (2020). Moreover, the detailed

140 implementation of the fracturing module used in this study can be found in Fu et al. (2013) and

141 Settgast et al. (2017).

142

2.1 Governing equations of the THM model

144 As presented in Fig.1, we consider a permeable body Ω bounded by the external boundary Γ that

145 contains Dirichlet and Neumann boundary conditions for geomechanical (traction boundary Γ_t

146 and displacement boundary Γ_u) and flow problems (prescribed pressure/temperature boundary

147 Γ_{PT} and flux boundary Γ_F), respectively. Specifically, for the geomechanical problem, Γ is

148 subjected to the prescribed traction $\bar{t}$ and displacement $\bar{u}$ applied on Γ_t and Γ_u, respectively. For

149 the flow problem, prescribed thermodynamic conditions such as pressure $\bar{P}$, and fluxes of mass

150 or heat ($\bar{F}$) are applied on Γ_{PT} and Γ_F, respectively.

151 Domain Ω also contains an internal boundary Γ_f, where boundary conditions corresponding to a

152 growing fluid-driven fracture in response to the injected mass q_{inj} are applied. Γ_f describes the

153 fracture whose unit direction vector $\boldsymbol{n}_f$ is orthogonal to Γ_f and consists of two opposing surfaces

154 Γ_f^+ and Γ_f^- as shown in Fig.1. The body is assumed to be permeable so that leakage $\boldsymbol{F}_f$ can occur

155 from the fracture to the surrounding body through Γ_f if a positive pressure difference from the

156 fracture to the body is present or vice versa. Note that the process of leakoff is illustrated in the

157 enlarged inset in Fig.1.

158
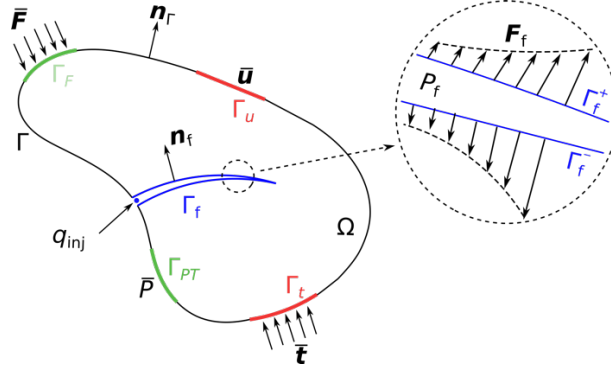
Fig. 1. Conceptual schema for modeling the evolution of a fluid-driven fracture in a permeable medium. Ω is a permeable body with an external boundary Γ that contains Dirichlet and Neumann boundary conditions for both geomechanical and flow problems. The evolving fracture in response to the injection fluid of q_{inj} is represented as an internal boundary Γ_f, highlighted in blue. The enlarged inset illustrates the leakoff of fluids F_f in the fracture through Γ_f.

The reservoir rock and the overlaying/underlying rocks (both caprock and basement) are treated as porous media subjected to fluid/heat flow as well as poromechanical deformation. The mathematical formulations and discretization strategy of the THM model are based on the following set of assumptions and treatments.

- For the fluid flow and heat transfer model, the movements of mobile phases through fractures and matrix are assumed to follow lubrication theory (Witherspoon et al., 1980) and Darcy's law, respectively.

- For the geomechanical model, the deformation of porous rock matrix is assumed to be quasi-static and linearly elastic. We use the small deformation assumption for the stress-strain relationship.

- Fractures and porous matrix are represented using separate but associated meshes: Fractures are represented with planar elements in the 3D space while the matrix is

176 represented with solid elements. A mapping between the two meshes is generated as the

177 solid mesh is split to create the fracture mesh.

178 Additional assumptions and treatments associated with multiphase flow and heat transport model

179 are identical to ones adopted in Fu et al. (2020).

180

181 **2.1.1 Geomechanical model**

182 The governing equations for quasi-static solid deformation of a permeable body Ω can be

183 expressed as

185
$$\nabla \cdot \boldsymbol{\sigma} + \rho_{\mathrm{m}}\mathbf{g} = \mathbf{0}$$

184   (1)

186 where $\nabla \cdot$ is the divergence operator; $\boldsymbol{\sigma}$ is the second-order total stress tensor; $\mathbf{g}$ is the gravity

187 vector; and $\rho_{\mathrm{m}} = \phi \sum_{J=\mathrm{A,G}} S_J \rho_J + (1 - \phi)\rho_{\mathrm{s}}$ is the bulk density of matrix, in which subscript J

188 denotes a phase of component in porous media (i.e., the aqueous (A) or gaseous (G) phase), S_J is

189 the saturation of phase J, ρ_{s} is the grain density, and ϕ is the true porosity, defined as the ratio of

190 the pore volume to the bulk volume in the deformed configuration (Kim et al., 2011).

191 Based on the thermo-poroelasticity theory (Biot 1941; Coussy 2004) and the assumptions of

192 linearly elastic and small deformation, $\boldsymbol{\sigma}$ can be related to the temperature field and displacement

193 field:

195
$$\boldsymbol{\sigma} = \boldsymbol{C}_{dr} : \nabla \boldsymbol{u} - bP_{\mathrm{E}}\mathbf{1} - 3\alpha_{\mathrm{L}}K_{\mathrm{dr}}dT\mathbf{1}$$

194   (2)

196   where $\boldsymbol{C}_{dr}$ is a fourth-order elastic tensor, associated with the drained-isothermal elastic moduli;

197   ∇ is the gradient operator; $\boldsymbol{u}$ is the solid displacement vector, also the primary unknown of the

198   geomechanical model; b is Biot's coefficient; $\mathbf{1}$ is a second-order identity tensor; α_{L} is the linear

199   coefficient of thermal expansion; K_{dr} is the drained-isothermal bulk modulus; $P_{\mathrm{E}} = \sum_J S_J P_J -$

200   $\int_{S_A}^1 P_{\mathrm{c}}(S)\mathrm{d}S$ is the equivalent pore pressure (Coussy 2004), in which P_J is the fluid pressure of

201   phase J and P_{c} is the gas-water capillary pressure as a function of aqueous saturation; and $dT =$

202   $T - T_{\mathrm{ref}}$ is the temperature difference, in which T is the current temperature and T_{ref} is a

203   reference temperature.

204   In the geomechanical model, we consider the fluid pressure in the fracture, P_{f}, as a normal

205   traction exerted on the fracture faces, Γ_{f}, while we neglect the shearing traction of the fluid on

206   solid matrix. Therefore, the traction balance across the fracture surface can be written as

207   $\boldsymbol{t}_{\mathrm{f}} = -P_{\mathrm{f}}\boldsymbol{n}_{\mathrm{f}}$ on Γ_{f} (3)

208   The external boundary conditions, traction and kinematic, are governed by

209   $\bar{\boldsymbol{t}} = \boldsymbol{\sigma}\boldsymbol{n}_t$ on Γ_t, (4)

210   $\bar{\boldsymbol{u}} = \boldsymbol{u}$ on Γ_u, (5)

211   Where $\boldsymbol{n}_{\mathrm{f}}$ and $\boldsymbol{n}_t$ are the normal unit vectors on Γ_{f} and Γ_t, respectively; $\bar{\boldsymbol{u}}$ is the prescribed

212   displacement on Γ_u.

213

214   **2.1.2   Multiphase multicomponent flow and heat transfer model**

215   The formulations of mass-and-energy conservation can be expressed in a unified

216   integrodifferential form as:

217
$$\frac{d}{dt}\int_{\Omega_\alpha} M_\alpha^\kappa \, d\Omega_\alpha + \int_{\Gamma_\alpha} \boldsymbol{F}_\alpha^\kappa \cdot \boldsymbol{n} \, d\Gamma_\alpha = \int_{\Omega_\alpha} q_\alpha^\kappa \, d\Omega_\alpha, \quad \kappa \equiv c, w, \theta; \quad \alpha \equiv m, f$$

218   (6)

219   where subscript α denotes a type of flow model (i.e., matrix flow model when $\alpha = $ m, and

220   fracture flow model when $\alpha = $ f); superscript κ denotes a component (i.e., CO_2 when $\kappa = $ c, and

221   water when $\kappa = $ w) or heat (when $\kappa = \theta$) in porous media, respectively.

222   For the matrix flow model ($\alpha = $ m), the formulation is identical to the one given by Fu et al.

223   (2020). For the fracture flow model ($\alpha = $ f), the mass-and-heat accumulation term M_f^κ integrating

224   over an arbitrary volume of a fracture is given by:

225
$$M_f^\kappa = \begin{cases} \int_{\Gamma_f} \sum_{J=A,G} S_J \rho_J X_J^\kappa w^h \, d\Gamma_f & \kappa \equiv c, w \\[2em] \int_{\Gamma_f} \sum_{J=A,G} S_J \rho_J U_J \, d\Gamma_f & \kappa \equiv \theta \end{cases}$$

226   (7)

227   where X_J^κ, ρ_J, and U_J denote the mass fraction of component κ, the density, the specific internal

228   energy of phase J, respectively. The volume of a fracture Ω_f is assumed to be the integral of the

229   product between its surface area Γ_f and hydraulic aperture w^h, represented by the gray volume in

230   Fig. 2(a), which can be expressed as:

232
$$w^h = (\boldsymbol{u}^+ - \boldsymbol{u}^-) \cdot \boldsymbol{n}_f$$

231   (8)

233   where $\boldsymbol{u}^+ - \boldsymbol{u}^-$ is the discontinuity in the displacement field across Γ_f. Eq. (8) provides a direct

234   coupling between the displacement field and the fracture flow.

235 Employing the assumption of the lubrication theory and accounting heat advection for fluid flow

236 in fractures, yields the mass-and-heat fluxes term of different components, $\boldsymbol{F}_f^{\kappa}$, written as

237
$$\boldsymbol{F}_f^{\kappa} = \begin{cases} -\sum\limits_{J=A,G} \rho_J X_J^{\kappa} \dfrac{(w^h)^2}{12\mu_J} \nabla P_J & \kappa \equiv c, w \\[2em] -\sum\limits_{J=A,G} h_J \rho_J \dfrac{(w^h)^2}{12\mu_J} \nabla P_J & \kappa \equiv \theta \end{cases}$$

238 $\hspace{11cm}$ (9)

239 where μ_J, ∇P_J, and h_J denote the dynamic viscosity of fluid, the fracture pressure gradient, the

240 specific enthalpy of phase J, respectively. All mass-and-heat fluxes through a fracture surface are

241 determined via looping through its edges and summing fluxes from its neighboring surfaces. The

242 transmissivity between fracture surfaces of different aperture is computed following the

243 treatment given in Pruess and Tsang (1990).

244 The mass-and-heat fluxes due to leakoff processes (as illustrated in the inset of Fig.1) can be

245 written, using Darcy's law by assuming a Newtonian flow, as:

246
$$\boldsymbol{F}_{\alpha}^{\kappa} = \begin{cases} -\sum\limits_{J=A,G} \rho_J X_J^{\kappa} \dfrac{k_J^r}{\mu_J} \boldsymbol{k}(\nabla P_J - \rho_J \boldsymbol{g}) & \kappa \equiv c, w \\[2em] -\boldsymbol{k}_{\theta} \nabla T - \sum\limits_{J=A,G} h_J \rho_J \dfrac{k_J^r}{\mu_J} \boldsymbol{k}(\nabla P_J - \rho_J \boldsymbol{g}) & \kappa \equiv \theta \end{cases}$$

247 $\hspace{11cm}$ (10)

248 where $\boldsymbol{k}$ and $\boldsymbol{k}_{\theta}$ denote the intrinsic permeability and the thermal conductivity of matrix elements

249 adjacent to a fracture face, respectively. Eq. (10) shows the transmissivity of the leakoff term

250 principally depends on the hydraulic properties of the matrix elements and the corresponding

251 leak-off area is equal to Γ_f. Eq. (10) also manifests that the fluid-and-heat leakoff in the matrix-

252 fracture flow is treated implicitly and 3D in nature.

253 For the component of water in the aqueous phase, the Dirichlet (in terms of fluid pressure $\bar{P}$) and

254 Neumann boundary conditions (in terms of mass flux $\bar{F}$) for the coupled thermo-hydro problem

255 can be expressed as follow:

256 $\bar{F} = \boldsymbol{F}_\alpha^w \boldsymbol{n}_F$ on Γ_F, (11)

257 $\bar{P} = P_A$ on Γ_{PT}, (12)

258 where $\boldsymbol{n}_F$ is the normal unit vectors exerted onto Γ_F; Γ_F and Γ_{PT} are the fixed mass flux and fluid

259 pressure boundaries in the matrix, respectively.
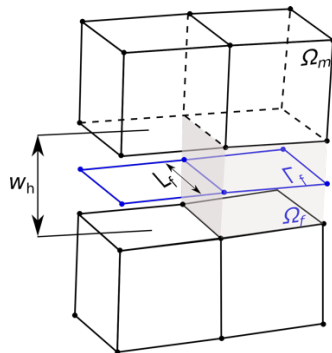
260

261 Fig. 2 Illustration of spatial discretization for coupled fracture-matrix flow model. Simulation domains of fracture

262 are displayed in blue, matrix domains in gray.

263

264 **2.1.3 Thermo-poromechanics**

265 We employ the fixed-stress iterative scheme to solve thermo-poromechanics in rock matrix (Kim

266 et al., 2011). In this scheme, the coupled THM problem splits into two subproblems, i.e. a fluid-

267 heat flow problem and a geomecahnical problem. During each iteration, the subproblems are

268 solved in an iterative sequence until the convergence of both problems. Particularly, in solving

269 the fluid-heat flow problem, the current true porosity is estimated from its previous state with the

270 following equation and assuming the rate of total volumetric stress remain unchanged throughout

271 the current time step.

$$d\phi = \frac{b - \phi}{K_{dr}}(dP_E + d\sigma_v) + 3\alpha_L b dT$$

272 (13)

274 where σ_v is volumetric total stress.

275 The numerical treatment of implementing the fixed-stress iterative scheme follows the same

276 procedure described in Fu et al. (2020).

277

278 **2.1.4 Fracture mechanics module**

279 We adopt the fracture mechanics module of GEOS, a high-performance computing simulation

280 code (Fu et al. 2013; Settgast et al. 2016; Ju et al., 2020), to simulate fracture propagation. This

281 module uses linear elastic fracture mechanics and a modified virtual crack closure technique

282 (MVCCT) to calculate energy release rate G at the fracture tip (Huang et al., 2019). The fracture

283 extends from the tip into intact rock when G exceeds the critical value G_c, which can be related

284 to the critical stress intensity factor K_{IC}, also known as fracture toughness, through

$$G_c = K_{Ic}^2(\frac{1 - v^2}{E})$$

285 (14)

287 When fracturing occurs, new fracture faces are created by splitting the nodes between the two

288 solid elements adjacent to the tip faces. As mentioned in the previous section, the fluid pressure

289 along the fracture is applied to the solid elements that are connected with those faces via a

290 normal traction force. Properly implementing this traction boundary condition is essential for

291   satisfying the momentum balance of solid elements in the updated mesh topology. Moreover, the

292   fluid-heat flow in newly created faces is automatically integrated into the matrix-fracture flow

293   system, ensuring mass-and-energy balance across the entire domain.

294   **2.2   The coupling scheme between the THM model and fracture mechanics module**

295   The three main components of our model, (1) the multiphase multi-component solver for porous

296   medium and fracture flow, (2) the hydraulic fracturing module, and (3) the poromechanics

297   solver, are all known to face their own numerical challenges (Kim and Moridis 2013; Settgast et

298   al., 2016; White et al., 2016). These modules are challenging even under less challenging

299   conditions, namely without the complication of fracturing for the first component and when the

300   latter two only deal with single-phase flow. In prior works, we have developed relatively robust

301   individual modules on a common platform, GEOS, for these three components (Settgast et al.,

302   2016; Fu et al., 2020). Still, coupling these three components together is a challenging task.

303   It is widely acknowledged that an implicit coupling strategy theoretically provides

304   unconditionally convergent numerical solutions and enables large timesteps for the preceding

305   coupled problem (Kim et al., 2012; Girault et al., 2016). However, the actual implementation to

306   implicitly couple the three aforementioned modules faces practically insurmountable numerical

307   difficulties, exacerbated by challenges associated with the parallel computing environment.

308   Specifically, the fully coupled scheme simultaneously solves a massive global nonlinear system

309   that rigorously represents all complex processes and strong discontinuities associated with

310   multiphase flow and fracture propagation. This paradigm requires a unified high-fidelity flow-

311   geomechanics simulator with powerful linear solver systems, which results in massive software

312   development efforts and computational costs.

313   We therefore develop a sequential coupling scheme to take full advantage of existing modules in

314   GEOS. Meanwhile, as sequential coupling often suffers from poor convergence, we capitalize on

315   the inherent self-stabilizing features of leakoff-dominated fracturing to simplify the coupling

316   scheme.

317   In this scheme, we use a compositional reservoir simulator for the fluid-heat flow problem and a

318   standard Galerkin finite element method for geomechanics. As mentioned in section 2.1.4, the

319   fracture mechanics module evaluates the fracturing criterion as well as updates the solid mesh

320   and flow network once new fracture surfaces are generated. The sequential communication

321   between the THM model and fracture mechanics module is achieved by sharing key information,

322   such as fluid pressure in fractures and displacement fields, at every timestep (see Fig. 3). This

323   procedure can be performed without compromising the modularity of the code because only

324   minor modifications are required for existing individual modules.

325   The relationships among the physical processes involved in the problem are summarized in

326   Table 1. Several interactions have been implicitly handled in existing modules. For instance, the

327   fracture flow and matrix flow are solved together by unifying the fracture flow network and the

328   matrix flow mesh in a combined flow topology as shown in Fig. 2. In other words, in the cell-

329   centered finite volume framework, both the flow "faces" for fracture flow and the solid

330   "elements" for matrix flow are considered "cells" interconnected together. Also, the solid

331   deformation and matrix flow are already coupled using the "fixed-stress" scheme in the

332   poromechanics solver. The remaining relationships are enforced sequentially as shown in Fig. 3.

333   As we will now explain, an inconsistency and thereby an error are introduced in the coupled

334   solution flow. In the nth iteration of each time step, the mechanical aperture, w_{m}, is computed in

335   Steps 3 (see Fig. 3) based on the geomechanical module's results. Step 4 then updates the

336   hydraulic aperture, w_h, which is defined as the arithmetic average of w_m by assuming that the

337   viscous loss along the fracture is negligible. In iteration $n+1$'s Step 1, a newton method is

338   employed to update w_h with solved fluid fields from previous timestep being the initial

339   guess. The derivative of w_h with respect to w_m is computed numerically by adding a small

340   perturbation to the initial guess of w_m. After each iteration, the fluid system will be reversed as a

341   new guess with updated w_h and solved fluid fields for next newton iteration. Therefore, the

342   aperture update in iteration n would introduce a small extra (positive or negative) fluid mass to

343   the system. We found this treatment is greatly beneficial for the convergence of the solution for

344   the following reason. An open fracture's aperture is extremely sensitive to fluid pressure. If we

345   use the fluid mass in each fracture cell from iteration n's Step 1 while using the updated aperture,

346   the initial "guess" of the flow system's state in iteration $n+1$ would be highly volatile and usually

347   far from the "true" solution, resulting in severe convergence difficulties. We hypothesize that the

348   fluid mass inconsistency is inconsequential for the overall accuracy of the solved system because

349   only a very small fraction of the injection fluid is stored in the fracture, a salient feature of the

350   leakoff-dominated regime. In the verification solution in Section 3 and simulation results in

351   Section 4, we compare the total masses of CO_2 in the numerical models with the total injected

352   quantities to quantify the induced error. Note that rock porosity is not very sensitive to pressure

353   change, so this treatment is unnecessary for the rock matrix cells.

354   Table 1. Coupling relationships between individual modules. The "step" in each cell refers to an "operation" in the

355   flow diagram in Fig. 3 where the interaction is embodied.

Modules providing information	Modules receiving information			
	Fracture Flow	Matrix flow	Solid deformation	Fracture mechanics

	Fracture Flow	Matrix flow	Solid deformation	Fracture mechanics
Fracture Flow	Self	Pressure boundary condition along fracture faces; solved together.	Traction boundary condition along fracture faces. Step 2.	Indirect influence, through solid deformation
Matrix flow	Fluid leakoff; solved together	Self	Solved together in poromechanics	Indirect influence, through solid deformation
Solid deformation	Hydraulic aperture and fluid storage. Step 4.	Solved together in poromechanics	Self	Compute energy release rate. Step 0.
Fracture mechanics	New fracture flow elements. Step 0.	Indirect influence, through fracture flow	Updated mesh. Step 0.	Self

356 We found the sequential coupling scheme to have satisfactory numerical performance: Most time

357 steps converge within several iterations; The scheme is stable provided the time step is

358 significantly smaller than the time that it takes the fracture to propagate the distance of one-

359 element length. This is again largely owing to the self-stabilizing features of fracture

360 propagation in the leakoff-dominated regime: As the permeability of the reservoir is largely

361 constant, the leakoff rate is mostly determined by the difference between fluid pressure in the

362 fracture and the far-field fluid pressure in the reservoir. In a propagating fracture, the fluid

363 pressure is marginally higher than the "fracture propagation pressure" near the fracture front. The

364 fracture opening pressure is in turn determined by the total stress in the system, which evolves

365 very slowly. Therefore, a convergent numerical solution can be obtained as long as the effects of

366 the extending fracture surface area on the flow into the rock matrix are captured.

367   The appropriateness of the simplified coupling scheme only relies on the dominant role of

368   leakoff in fracture propagation. Both viscous pressure loss and energy dissipation due to rock's

369   toughness are captured by the numerical formulation. Therefore, the model works in both the

370   toughness-leakoff regime and viscosity-leakoff regime as well the intermediate scenarios

371   (Dontsov, 2016).
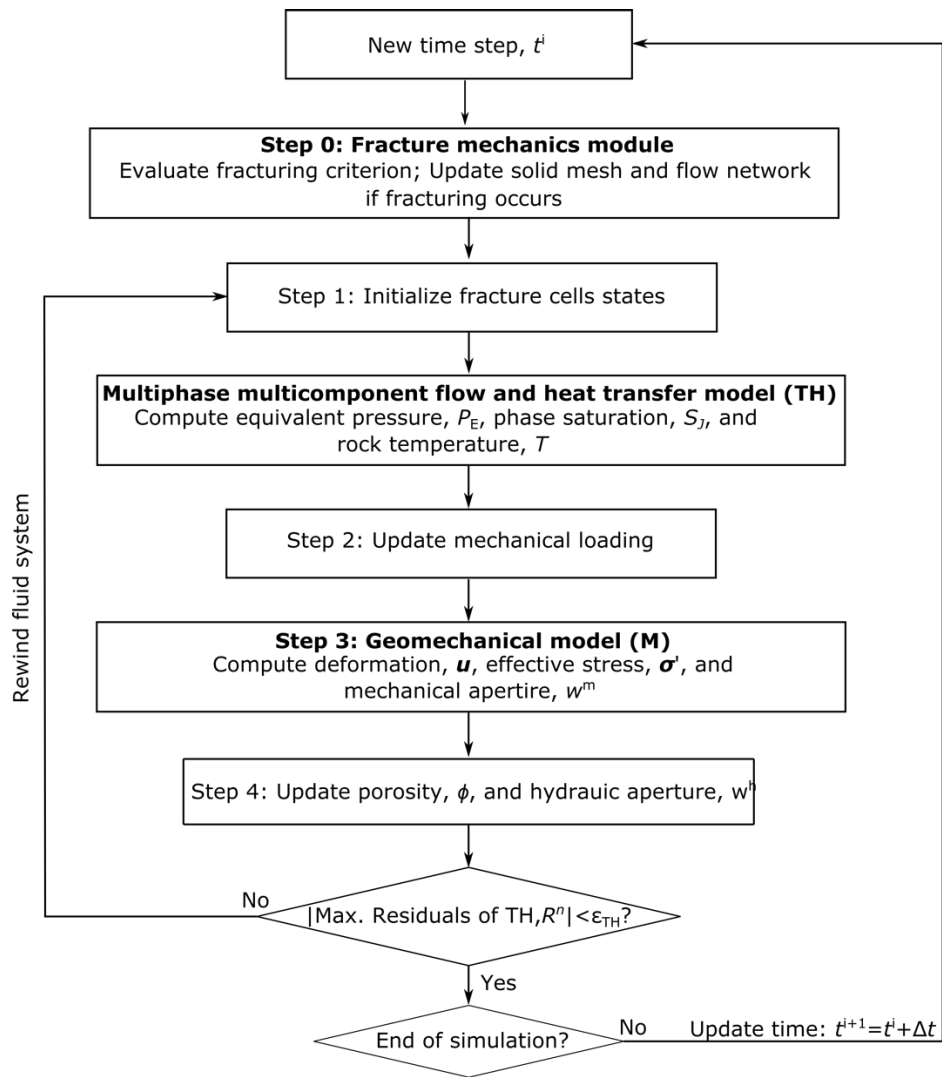
372

373   Fig. 3. Flowchart of the coupling scheme between coupled THM coupled model and fracture mechanics module.

374   The coupling convergence criterion of coupled THM model is that the maximum residuals of TH model is smaller

375   than ε, a pre-set small value, say 10^{-5}, after updating perturbed hydraulic variables.

376 **3 Verification**

377 In this section, we compare the new model's results with the PKN solution in the leakoff-

378 dominated regime to verify the numerical implementation of the model and, particularly, to

379 validate the coupling scheme presented in Section 2.2.2. Note that the validation of relevant

380 individual submodules in GEOS has been reported in previous works, in which numerical results

381 are compared with the analytical solutions of poromechanics (Terzaghi's and Mandel's problems

382 (Fu et al., 2019; Fu et al., 2020)), and of fracturing propagation in different regimes (Fu et al.,

383 2013; Settgast et al., 2017).

384

385 **3.1 The PKN solution in the leakoff-dominated regime**

386 We use a standard fracture geometry, the PKN model as illustrated in Fig. 4(a), to test the

387 proposed coupling scheme (Perkins and Kern 1961; Nordgren 1972). The origin of the

388 coordinate system is set at the injection point; the x-direction coincides with the fracture

389 propagation direction, so the y-axis is along the direction of the minimum principal *in situ* stress

390 S_{hmin}. Recall that hydraulic fracturing in a storage reservoir with moderate permeability is in the

391 leakoff-dominated regime. We therefore compare the numerical solutions against the PKN model

392 in the so-called leakoff-dominated regime (Nordgren 1972). This solution describes the growth

393 of a fixed-height vertical fracture when the volume of fluid loss into the reservoir is much larger

394 than the volume stored in the fracture.

395 According to the analytical solution (Nordgren 1972), the half fracture length L_f and aperture w_0^h

396 at the wellbore are

397
$$L_f = \frac{qt^{1/2}}{2\pi C_L h_f}$$

398   (15)

$$w_0^h = 4\left[\frac{\mu q^2}{\pi^3 E' C_L h_f}\right]^{\frac{1}{4}} t^{1/8}$$

400

399   (16)

401   where q is the total injection rate; h_f is the fracture height; $E' = E/(1-v^2)$ is the plane-strain

402   modulus for the formation; and C_L is the Carter's leakoff coefficient. As revealed in Howard and

403   Fast (1957), C_L can be expressed as:

$$C_L = \Delta P(\frac{k_r \phi c_t}{\pi \mu})^{1/2}$$

405

404   (17)

406   where ΔP is the difference between the fracture pressure and the remote reservoir pressure that is

407   assumed to be constant; k_r is the intrinsic permeability of the reservoir; and $c_t = c_f + c_p$ is the total

408   compressibility, where c_f is fluid compressibility and c_p is pore compressibility, both of which

409   are constants in equation (17). However, in a high-fidelity numerical model, c_f and c_p

410   respectively depend on the nonlinear PVT properties of fluids and the solid deformation in the

411   coupled THM models. Therefore, when applying the analytical solution, we set c_t to the value

412   computed from the numerical models for simplicity. Also note that equation (17) assumes 1D

413   diffusion, which is not necessarily valid in a real reservoir or in a high-fidelity numerical model.

414   Some additional, special adaptations of the numerical model are needed to be consistent with

415   assumptions of the analytical solution. The analytical solution intrinsically assumes zero

416   toughness for the reservoir rock. Accordingly, we set the toughness of reservoir rock to

417   100 Pa•m$^{0.5}$, a small finite value that prevents small numerical noise from triggering fracturing

418   artificially. The analytical solution calculates leakoff using Carter's leakoff coefficient, which is

419   based on 1D diffusion. However, the fluid flow in the THM coupled model is 3D in nature. To

420   match the 1D diffusion assumption, we use a strongly anisotropic permeability (k_{ry}=10 mD,

421   k_{rx}=k_{rz}=0 mD). We also run an additional simulation by removing the 1D diffusion restriction for

422   comparison. Moreover, the Biot coefficient is set to zero in the numerical model, since the PKN

423   model does not incorporate the poromechanical effects in the reservoir. Note that none of the

424   above adaptations is used in the 3D simulations in section 4 and beyond.
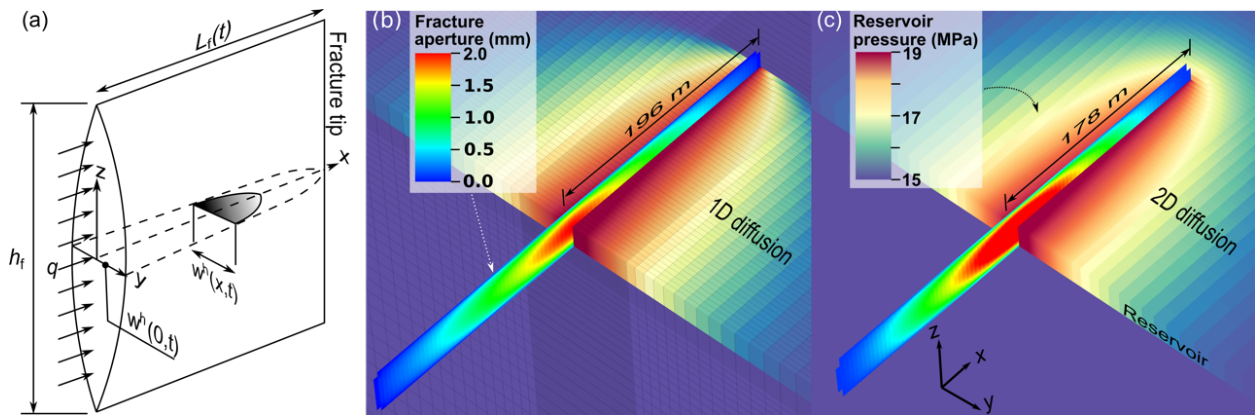
426   Fig. 4. Geometrical characteristics (a) and simulation results for a PKN fracture with q=0.04 m³/s in the case of (b)

427   1D diffusion and (c) 2D diffusion at t=4×10⁵s. In (a) where only one wing of the fracture is shown due to symmetry,

428   h_f, q, w^h, and L_f indicate fracture height, injection rate, fracture width (aperture), and fracture length, respectively. In

429   (b) and (c), a full length/height of the fracture and a quarter of the reservoir pressure field are presented. Note that

430   fracture color scale indicates fracture aperture, whereas the color scale for the matrix indicates reservoir pressure.

3.2   Numerical realization of the PKN model

432   The numerical simulation only models one quarter of the problem owing to the symmetrical

433   condition of PKN model, as shown in Fig. 4(a). To minimize boundary effects, the dimensions of

434   the quarter model are 1000 m, 2000 m, and 1000 m in x-, y-, and z-directions, respectively,

435   where meshing in each dimension contains a refined portion (200 m, 100 m, and 40 m in x-, y-,

436   and z-directions, respectively) and coarse portion. The refined region uses constant mesh

437   resolutions in three directions, i.e. 4 m, 1 m, and 2 m, respectively, whereas the coarse region

438   uses a progressively coarser mesh resolution toward the far-field. The model is discretized into

439   1,004,731 hexagonal elements. We simulate fracture propagation and reservoir response for three

440   different injection rates as listed in Table 1. The fourth simulation removes the 1D diffusion

441   restriction for the baseline injection rate and results are denoted by "2D diffusion" in Fig. 4 and

442   5. Parameters adopted in the verification are listed in Table 1.

443

444   Table 1. Parameters employed in the numerical model for the simulation of the PKN model.

Property	Value
Fracture height, H_f	40 m
Injection rate, q	0.02, 0.04[a], and 0.06 m^3/s
Dynamic viscosity, fluid, μ	1×10^{-3} Pa s
Porosity, ϕ	0.2
Pore compressibility, c_t	1.04×10^{-8} Pa^{-1}
Poisson's ratio, v	0.25
Biot's coefficient, b	0.0
Carter's leakoff coefficient, C_L	0.493 mm/$\sqrt{s}$
Young's modulus, E	10 GPa
Critical stress intensity factor (toughness), reservoir	100.0 Pa•m$^{0.5}$

445   [a]baseline case simulation

446

447   **3.3   Verification results**

448   Fig. 5 shows a comparison of results from the numerical simulation and the PKN solutions. In

449   general, the temporal evolution of fracture length for the three injection rates are in good

450   agreement with the corresponding analytical solutions. The numerically simulated apertures tend

451   to deviate from the analytical solutions early in the injection but gradually converge to the

452   solutions as injection progresses.

453   The disparity between the numerical solution and the PKN solution at the early times is likely

454   caused by the geometric assumptions of the PKN model, i.e. the fracture length being much

455   larger than the fixed fracture height (a rectangular fracture shape). In the early stage of injection,

456   the fracture length simulated by the numerical model, however, is smaller than or similar to the

457   preset fracture height, forming a penny shape and therefore a direct comparison between

458   solutions with different fracture shape assumptions is not appropriate. Note that for all the three

459   injection rates, the numerically predicted apertures become very similar to the analytical

460   solutions when the half fracture length in each case reaches around 200 m, 2.5 times the fracture

461   height. Fig. 5(b) also shows that numerical results of wellbore aperture exhibit a moderate

462   oscillatory behavior. This behavior is expected because the spatial discretization scheme dictates

463   that the fracture has to propagate by the length of an element, yielding numerical

464   overshoot/undershoot.

465   As shown in Fig. 5(c), the percentage of fluid in the fracture compared with the total injection

466   volume, termed "*fracture volume ratio*" in this study, is quite low, generally less than 1%. This

467   confirms that these four simulated hydraulic fractures are indeed in the leakoff-dominated

468   regime. Note that the "fracture volume ratio" is mathematically identical to the "fluid efficiency"

469   used in unconventional reservoir stimulation. However, we avoid using this established term

470   because in carbon storage, retaining more fluid in the fracture, i.e. achieving a "high fluid

471   efficiency", is not an objective.

472   Fig. 5(d) shows the temporal evolution of "*mass loss ratio*", defined as the percentage of mass

473   loss induced by the coupling scheme compared with total injection mass in this study. Note that a

474   negative mass loss ratio means extra masses are introduced in the system. A small yet noticeable

475   error is introduced at early time by the inconsistency in the coupling scheme. However, this

476   inconsistency rapidly diminishes, and the absolute mass losses converge to near 0.05 % as the

477   leakoff dominates. The convergence of mass loss ratio for each case validates our hypothesis that

478   the mass loss induced during the coupling is indeed trivial and proves the accuracy of our

479   coupling scheme for simulating leakoff-dominated fracturing.

480   The comparison between Fig. 4(b) and (c) shows the fracture length grows faster in the case of

481   1D diffusion than that of 2D diffusion where the reservoir pressure plume front goes farther than

482   the crack tip. Likewise, Fig.5 (a) and (c) shows that the case of 2D diffusion yields a slightly

483   higher leakoff compared with the baseline verification (1D diffusion), which includes lower

484   fracture growth rate and smaller wellbore aperture. Those behaviors are mainly owing to the

485   overestimation of the actual C_L when 2D diffusion is invoked (Carrier and Grant, 2010; Fu et al.,

486   2017).
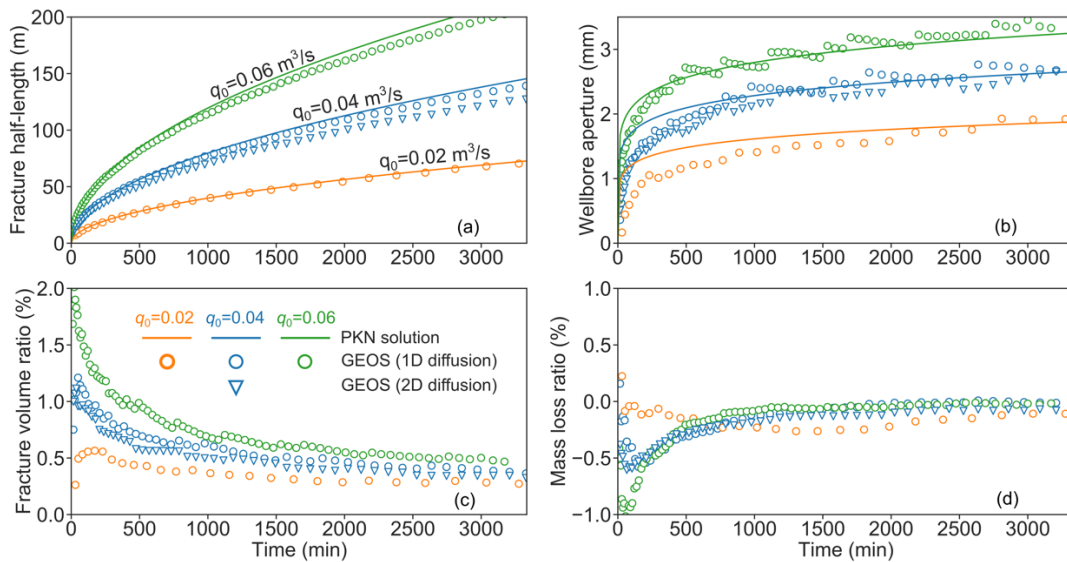
487

488   Fig. 5. Simulation results for a PKN fracture in the leakoff-dominated regime. (a), (b), (c) and (d) plot the temporal

489   variations of fracture half-length, wellbore aperture, fracture volume ratio, and mass loss ratio respectively.

490   Analytical solutions for leakoff-dominated fractures are plotted in (a) and (b) for comparison. The fracture volume

491   ratio in (c) denotes the percentage of the total injected fluid stored in the fracture. The mass loss ratio in (d) denotes

492   the percentage of the mass loss induced by the coupling scheme compared with the total injection mass.

493   **4   Application in simulating fracturing into caprock**

494   To demonstrate the capabilities of the proposed scheme and apply it to GCS, we build and

495   analyze a field-scale 3D numerical model (hereafter referred to as the baseline case) in GEOS in

496   this section. The baseline model is loosely based on the geological settings of the In Salah

497   storage site (Rutqvist et al., 2010; Ringrose et al., 2013; White et al., 2014), as shown in Fig. 6

498   (a), while the analyses generally apply to a GCS reservoir with marginal permeability.

499
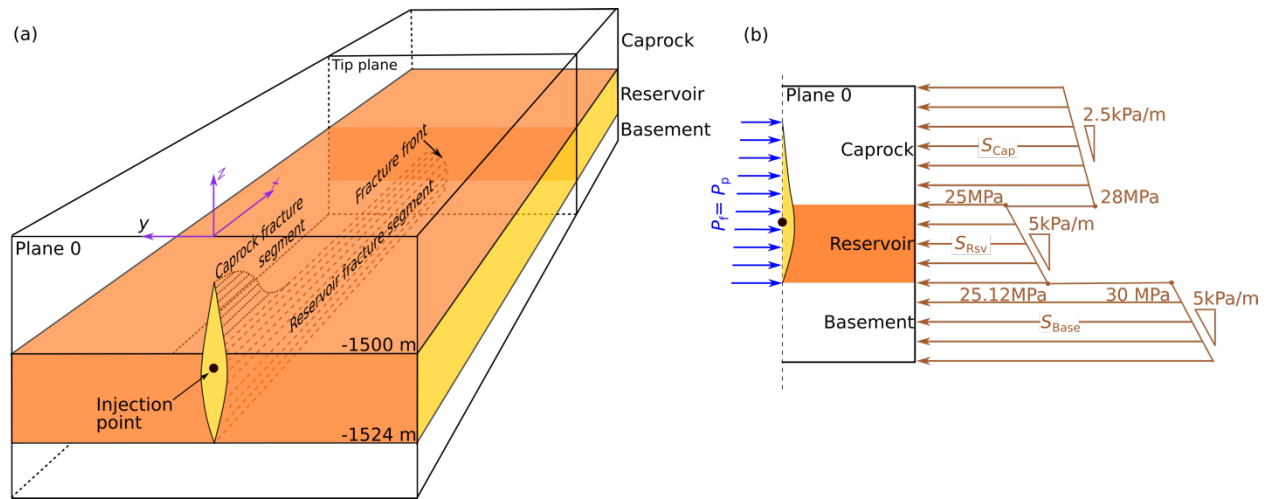
500   Fig. 6. (a) 3D schematic (not to scale) of the configuration, geometry and dimensions of the baseline model showing

501   one wing of a hydraulic fracture penetrating into the caprock, with cold supercritical CO_2 entering the computational

502   domain from the injection point, marked as a black dot on the plane 0 (x=0). Tip plane tracks the movement of

503   fracture front. Sub-figure (b) shows internal and external traction boundary conditions, i.e. fracture pressure and

504   horizontal *in-situ* stress, applied to the 3D model on plane 0. Note that only one wing of the fracture in panel (a) is

505   shown due to symmetry.

506

507   **4.1   Model setup**

508   Fig. 6(a) schematically depicts the 3D geometry of the baseline model. The CO_2 storage

509   reservoir of marginal permeability is sandwiched between the caprock and the basement, both of

510   which are much less permeable. The reservoir is 24 m thick with its interface with the caprock

511   located at 1500 m depth ($z = -1500$ m). We established a 3D coordinate system, in which the x-

512   axis is parallel to the direction of the maximum *in situ* horizontal stress (S_{Hmax}), the y-axis is

513   parallel to the direction of minimum *in situ* horizontal stress (S_{hmin}), the z-axis points upward,

514   and the origin at ground surface resides above the injection point. The injection point is

515   annotated as a black dot in Fig.6 (a) to highlight its position. Note that the vertical location of the

516   injection point should not alter the outcome of fracturing because there is no fracturing barrier

517   inside the reservoir. The initial pore pressure follows the hydrostatic distribution and the initial

518   reservoir temperature is set as 65 °C. The minimum principal *in situ* stress (S_{hmin}) follows a

519   segmented-linear distribution along the z direction, as shown in the right portion of Fig. 6(b).

520   S_{hmin} spatial distributions with caprock, reservoir, and basement layers are denoted by S_{Cap},

521   S_{Rsv}, and S_{Base}, respectively. We assume that there is a fracturing barrier between the reservoir

522   and basement that prevents downward fracturing as we mainly focus on conditions and

523   mechanisms for fracturing in the reservoir and caprock. As illustrated in Fig. 6(a), the fracture

524   propagation is assumed to only take place within the x-z plane, perpendicular to the direction of

525   S_{hmin}. Note that the symmetry of the system with respect to the y-z plane at the injection point

526   allows the use of a half model.

527   Fully-saturated supercritical CO_2 at an injection temperature of 45°C, is injected into the

528   reservoir at a constant rate of 15.0 kg/s (one wing of fracture), approximately a million metric

529   ton per year. We assume that the injection well is cased, and fractures are initiated from

530   perforations, which limits the well only to communicate with the system through the fracture.

531   Thus, the injection well can be simplified as a point source in our 3D computational domain. In

532   the initial state of a simulation, we pre-create a small fracture, usually 2x2 fracture elements in

533   size, to provide an inlet for injection. How a fracture is initiated due to CO_2 injection in a low-

534   permeability formation, with the presence of poro-mechanical effects, has been investigated by

535   Fu et al. (2020).

536   The so-called "roller" boundary condition is applied to all "far-field" boundaries of the

537   geomechanical model. For the fluid flow model, prescribed mass/heat rate conditions for the

538   injection well are applied at $x=0$, $y=0$ and $z=-1504$ m. We apply the original reservoir pressure

539   and a constant ambient temperature (65°C) at the lateral boundaries as the far-field Dirichlet

540   boundary conditions. No-flow conditions are applied to elements on the top and bottom planes.

541   The computational domain of the baseline case has a core region whose dimensions in x-, y-, and

542   z-directions are 800 m, 200 m, and 240 m, respectively. The core region has a relatively fine

543   mesh resolution of 8.0, 4.0, and 8.0 m in those directions. Surrounding the core region is a

544   coarsely resolved region that extends to 5800 m, ±9000 m, and ±400 m in the respect three

545   directions, which mitigates boundary effects while maintaining computational efficiency. The

546   baseline model involving a kilometer-scale reservoir and 3 years of injection time, is discretized

547   into 1,344,000 elements and the simulation is conducted across 252 CPU cores (16 Intel®

548   Xeon® E5-2670 CPUs), which runs for 18 hours on a high-performance computer (4536 core-

549   hours in total).

550   Table 3 summarizes the computational parameters and constitutive models for the baseline

551   model. As for the mobility-related constitutive models in multiphase flow model, we use a

552   Corey-type relative permeability functions (Brooks and Corey, 1964) and a van Genuchten

553   capillary function (Van Genuchten, 1980), respectively written as Eq. (18) and (19).

554     $k_A^r = S_n^4, k_G^r = (1 - S_n)^2(1 - S_n^2)$ (18)

555     $P_C = -P_0[(S^*)^{-1/\lambda} - 1]^{-1/\lambda}, S^* = (S_A - S_{irA})/(1.0 - S_{irA})$ (19)

556   where k_A^r and k_G^r are relative permeabilities in aqueous and gaseous phases; $S_n = (S_A -$

557     $S_{irA})/(1.0 - S_{irA} - S_{irG})$ is the normalized aqueous saturation; S_{irA} and S_{irG} are the irreducible

558   aqueous saturations and the residual gas saturations, respectively. λ and P_0 are the exponent that

559   characterizes the capillary pressure curve and the capillary modulus, respectively. Then, we set

560     $S_{irA} = 0.12$ and $S_{irG} = 0.01$ for relative permeability, and $S_{irA} = 0.11$, $P_0 = 12500$ Pa, and $\lambda =$

561   0.254 for capillarity, where the capillary pressure model employs a slightly smaller S_{irA} than the

562   model of relative permeability in order to prevent unphysical behavior (Moridis and Freeman,

563   2014).

564

565   Table 2. Parameters employed in the baseline simulation

Property	Baseline value
Reservoir thickness, H_r	24 m
Minimum principal *in situ* stress in reservoir, total stress, mid-depth, S_{hmin}^r	25 MPa
Minimum principal *in situ* stress in caprock, total stress, mid-depth, S_{hmin}^c	30 MPa
Initial pore pressure, mid-depth of reservoir, P_{int} (hydrostatic condition applies)	15 MPa
Biot's coefficient, reservoir rock, b_r	0.5
Biot's coefficient, caprock, b_c	0.25
Intrinsic permeability, reservoir, k_r	15 mD
Intrinsic permeability, other layers, k_c	0.1 μD

Porosity, reservoir, ϕ_r	0.15
Porosity, all other layers, ϕ_c	0.05
Young's modulus, all layers, E	10 GPa
Poisson's ratio, all layers (Armitage et al., 2010), v	0.25
Initial temperature, all layers, T_{Int}	65 °C
Coefficient of thermal expansion, linear, α_L	10^{-5} /°C
Injection temperature, T_{Inj}	40 °C
Thermal conductivity, all layers, λ	3.0 W/(m·K)
Heat capacity, all layers, C_s	1000 J/(kg·K)
Critical stress intensity factor (toughness), all layers (Senseny and Pfeifle, 1984)	1.0 MPa·m$^{0.5}$
Relative permeability model[a] (Brooks and Corey, 1964)	$k_A^r = S_n^4$ $k_G^r = (1 - S_n)^2(1 - S_n^2)$ $S_n = (S_A - S_{irA})/(1.0 - S_{irA} - S_{irG})$ $S_{irA} = 0.12$, $S_{irG} = 0.01$
Capillary pressure model[b] (Van Genuchten, 1980)	$P_C = -P_0[(S^*)^{-1/\lambda} - 1]^{-1/\lambda}$ $S^* = (S_A - S_{irA})/(1.0 - S_{irA})$ $S_{irA} = 0.11$, $P_0 = 12500$ Pa, $\lambda = 0.254$

566 a k_A^r and k_G^r are relative permeabilities in aqueous and gaseous phases; S_n is the normalized aqueous saturation; S_{irA}

567 and S_{irG} are the irreducible aqueous saturation and the residual gas saturation, respectively

568 b P_0 is the capillary modulus

569

4.2 Results of baseline model

571 As presented in Fig. 7 and Fig. 8, results of the baseline model clearly show how a leakoff-

572 dominated fracture is driven by injection and provides an evolving interface between injection

573 and reservoir storage. By the end of three years of injection, the fracture has propagated 620 m

574   into the reservoir, providing a growing interface plane for feeding injected CO_2 into the

575   reservoir. The CO_2 plume advances approximately 625 m in the y-direction on each side (Fig.

576   8(p)), spanning an area of reservoir as large as about 1.24×1.25 kilometers. Note that the rate of

577   injection employed in the baseline case cannot possibly be achieved if the downhole injection

578   pressure is strictly limited to below the estimated fracturing pressure of the caprock,

579   approximately 25 MPa. Meanwhile, the maximum fracture height only reaches 88 m, thereby

580   being vertically contained in the lower portion of the caprock (Fig. 7(b) and Fig. 8(m)). Note that

581   the containment mechanism will be elucidated in the subsequent analysis.
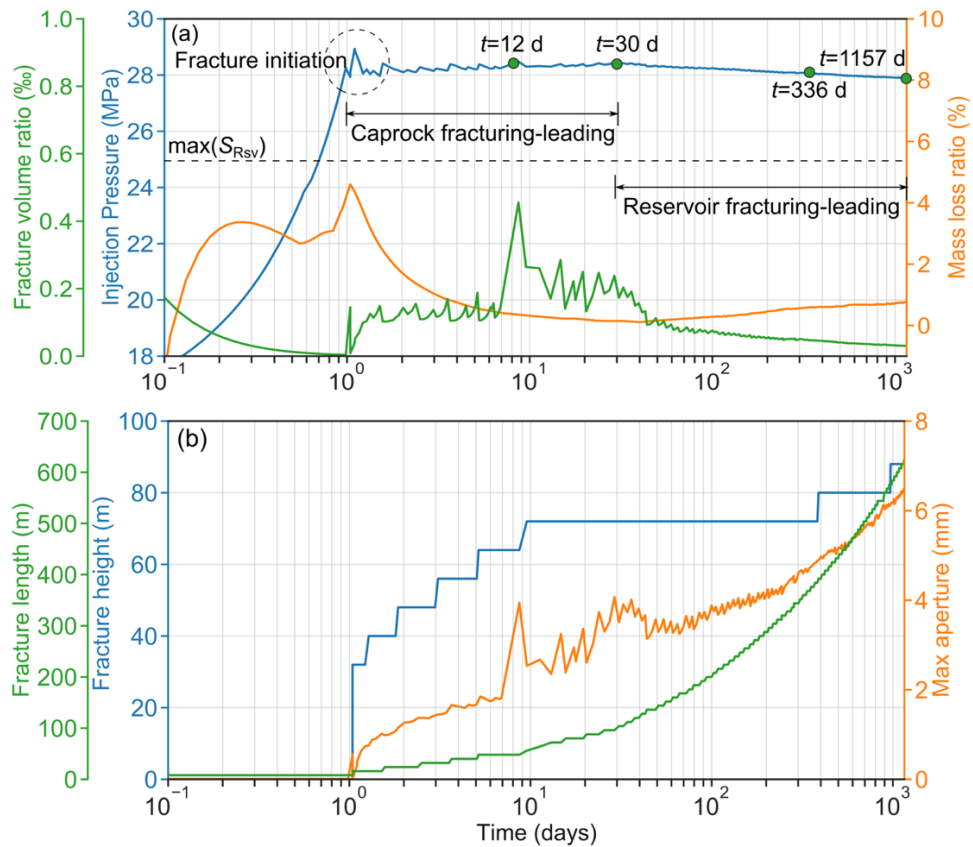
582

583   Fig. 7. Overall responses of the system in the baseline case. (a) Fracture volume ratio, injection pressure, and mass

584   loss ratio versus time; (b) Fracture length, fracture height, and max aperture versus time. The curve colors in (a) and

585   (b) correspond to their y axes. Fracture volume ratio is the percentage of injected fluid retained in the fracture.

586   Injection pressure is measured at the injection point at the entrance to the fracture. Mass loss ratio is the percentage

587   of injected CO_2 mass that is "lost" due to the error introduced by the sequential iteration scheme as explained in

588   section 3.3. Note that the highest stress level of S_{Rsv}, max(S_{Rsv}), which is the in situ stress magnitude at the bottom

589   of the reservoir, is indicated by a black dash line in (a).

590

591   Another interesting observation is the evolution of injection pressure (the blue line in Fig. 7(a))

592   at the entrance to the fracture over time, which can be divided into three stages: (1) the initially

593   rapid pressure buildup before apparent fracture growth (about 1 day), (2) the pressure plateau as

594   fracture propagates (from 1 day to 30 days), and (3) the subsequent slow pressure decline (after

595   30 days). In the first stage, accommodating the injection rate requires sustaining an open fracture

596   in the reservoir, which in turn requires a continuously increasing injection pressure, much higher

597   than original S_{Rsv}, owing to the effect of back-stresses caused by pressure diffusion into the

598   reservoir (Detournay and Cheng, 1997; Kovalyshen, 2010). Fu et al. (2020) had modeled how

599   this effect causes rapid increase of injection pressure and eventually causes fracturing of the

600   caprock.
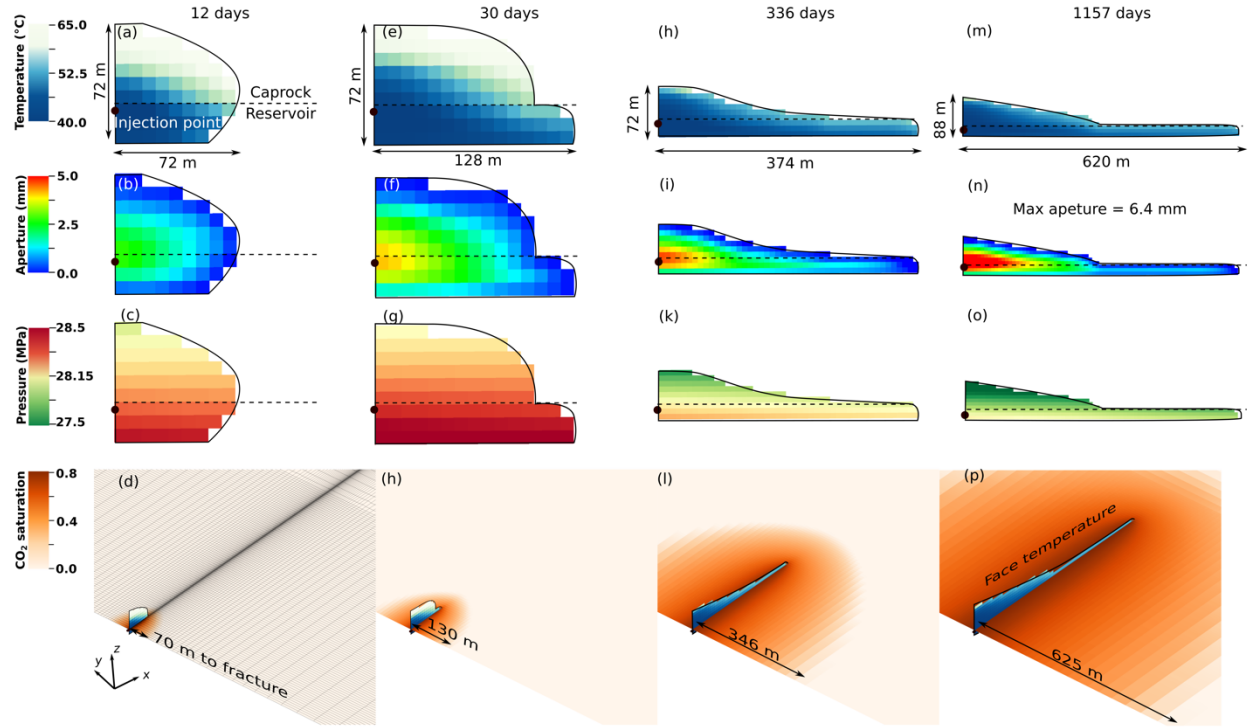
Fig. 8. Four selected states of the hydraulic fracture and the reservoir rock. The first three rows present snapshots of temperature (first row), aperture (second row), and pressure (third row) on the evolving hydraulic fracture. The last row shows the spatial-and-temporal evolution of CO_2 (critical state gas phase) in the reservoir (z=-1510 m). The interface between the reservoir and the caprock is denoted by a dark dashed line and the injection point is annotated as a black dot. Note that scales vary among the columns of the first three rows for clearer visualization, whereas the four sub-figures in the fourth row use the same scale.

Here we mainly focus on the evolution of fracture propagation after caprock fracturing takes place, which spans the second and third stages as designated in this section. Fig. 8 shows four representative states of the fluid-driven fracture and CO_2 saturation (supercritical state gas phase) in the reservoir rock, at 12 days (in second stage), 30 days (transition from second to third stage), 336 days and 1157 days (both in third stage). In the second stage when the pressure is largely constant, fracturing in caprock seems to lead fracturing in the storage reservoir. The constant injection pressure in this stage reflects the fracturing pressure of the caprock, which is mainly

616   influenced by S_{Cap}. Note that the injection pressure is only slightly higher than S_{Cap} near the

617   reservoir-caprock interface. In the third stage, reservoir fracturing leads the fracture length

618   growth and the injection pressure slowly declines as explained in Section 4.2.2. This pattern

619   change suggests an evolution of fundamental physical mechanisms that dominate fracture growth

620   as elucidated in the subsequent sections.

621

622   **4.2.1   Second stage: caprock fracturing-leading**

623   Fig. 9 presents spatial distributions of the fluid pressure, temperature, effective stress, and total

624   stress in two vertical cross-sections (near the injection and near the fracture tip, respectively) and

625   two horizontal cross-sections (in the reservoir rock 10 m below the bottom of the caprock, and in

626   the caprock 30 m above the top of the reservoir rock) after 12 days of injection. Pore pressure

627   propagates in the reservoir much farther than in the caprock, due to the much higher permeability

628   of the reservoir (150,000 times higher than that of the caprock). Significant temperature

629   decreases only take place within a short distance from the fracture in the reservoir (Fig. 9 (e) and

630   (f)), while temperature change in caprock is hardly perceptible (Fig. 9 (g)). Although thermo-

631   mechanical effect tends to reduce the total stress in the cooled region in the reservoir, the effect

632   of poroelasticity on increasing the total stress in this case is much stronger. As a result, the total

633   stress near the fracture in the reservoir even becomes higher than in the caprock, although initial

634   S_{hmin} in the reservoir was on average 3 MPa lower than that of the caprock. This reversed stress

635   contrast tends to hamper fracture propagation in the reservoir, favoring easier propagation in the

636   caprock.
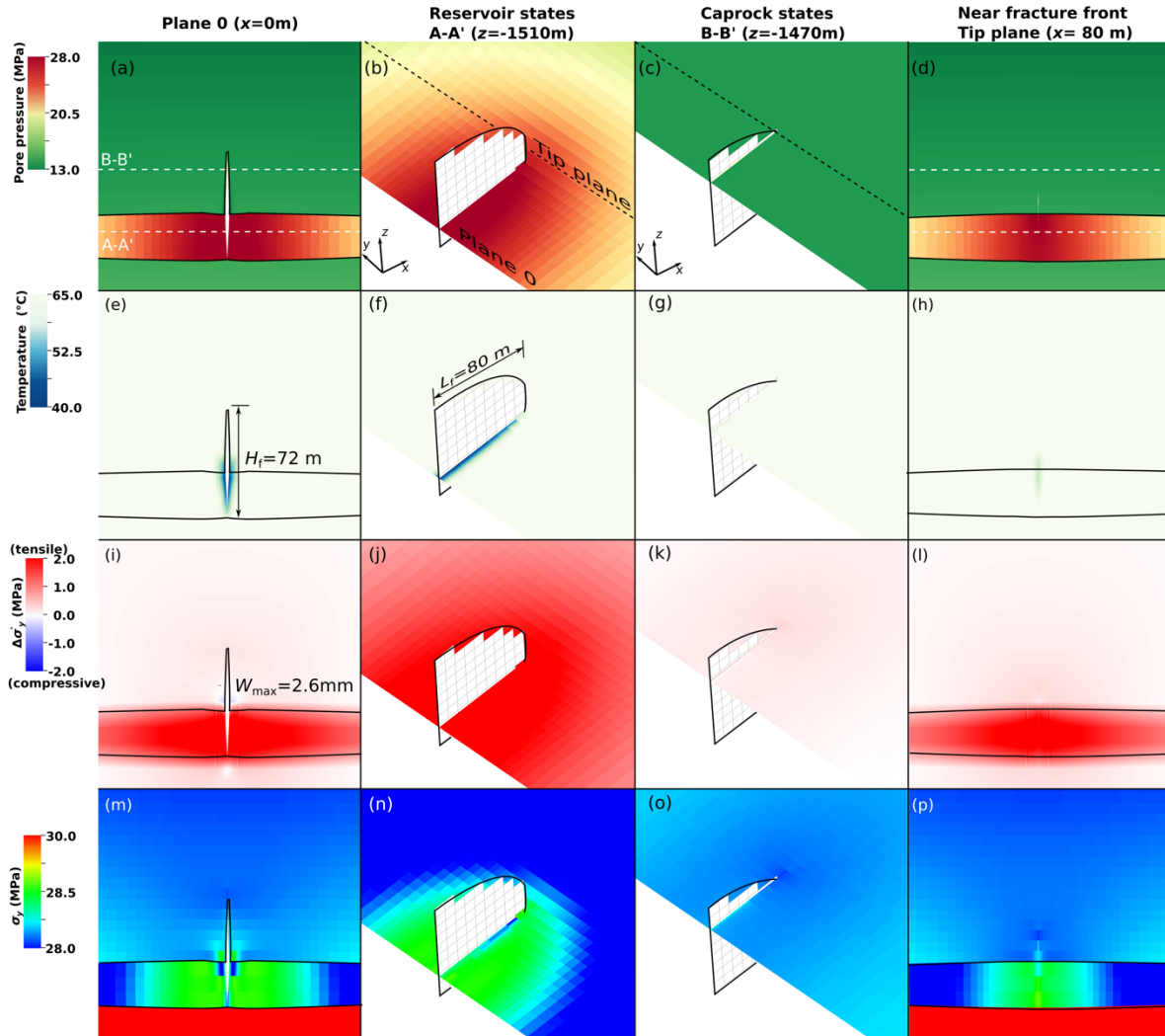
Fig. 9. States of the reservoir rock and the caprock after 12 days of injection. The four rows of panels show spatial distributions of pore pressure (first row), temperature (second row), effective stress increment (third row), and horizontal total stress (fourth row). The first and fourth columns respectively show the distributions of variables on two vertical planes cutting the injection point and the fracture tip, respectively. The second and third columns show the distributions of the variables on two horizontal planes A-A′ (reservoir) and B-B′ (caprock) respectively. The deformation of first and fourth columns is magnified by 500 times.

4.2.2 Third stage: reservoir fracture-leading stage

The system response in this stage is depicted using spatial distributions of the same variables as used in the preceding section but for a much later state, 1157 days into the injection (Fig. 10). In

648 general, the most marked difference from the second stage is that the fracture has horizontally

649 grown much longer, which mostly takes place in the reservoir rock, and that the cooling front in

650 the reservoir has advanced much farther (i.e. thermal penetration depth is comparable to fracture

651 height).
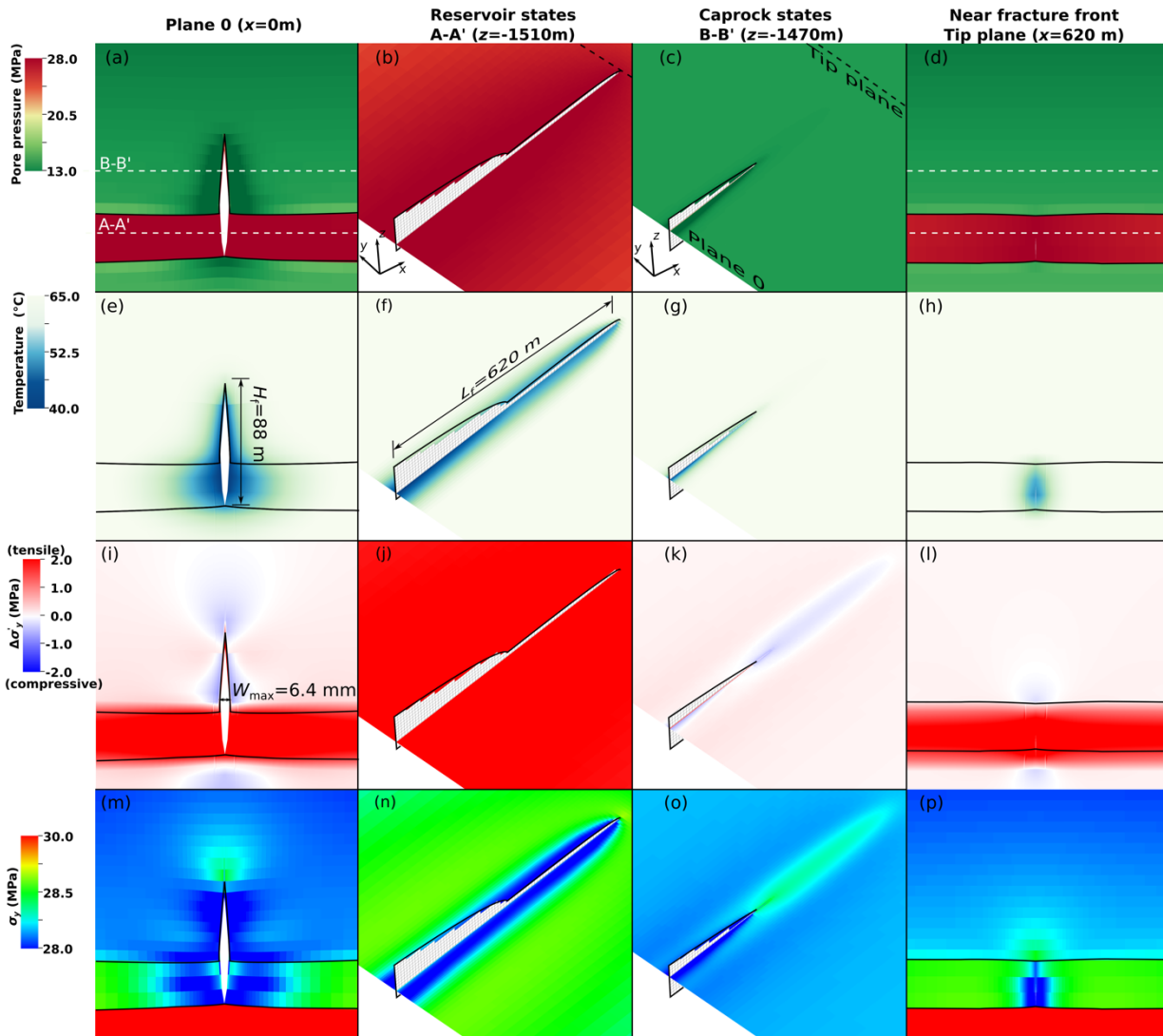
652

653 Fig. 10. States of the reservoir rock and the caprock after 1157 days of injection. The four rows of panels show

654 spatial distributions of four variables, namely pore pressure ((a) through (c)), temperature ((d) through (f)), effective

655 stress increment ((g) through (i)), and horizontal total stress ((j) through (i)). The first and fourth columns

656 respectively show the distributions of variables on two vertical planes cutting the injection point and the fracture tip,

657 respectively. The second and third columns show the distributions of the variables on two horizontal planes A-A′

658 (reservoir) and B-B′ (caprock) respectively. The deformation of first and fourth columns is magnified by 500 times.

659

660 Unlike the rapid and continuous horizontal propagation, the vertical propagation is slow and

661 contained, since only an absolute height growth of 16 m takes place throughout this stage (Fig.

662 10 (e) and Fig. 7 (b)). This vertical growth is mainly driven by the thermal contraction near the

663 injection point, which in effect decreases the original in-situ total stress (Fig. 10(o)). The growth

664 is expected to be slow since the dominant heat transfer mechanism in the caprock is heat

665 conduction, which itself is extremely slow. In addition, a favorable stress gradient contributes to

666 the vertical containment of the fracture. The adopted gradient of S_{hmin} such that $-dS_{hmin}/dz <$

667 $\rho_c g$ provides a relatively stable condition that halts the upward propagation. This is because it

668 takes more hydraulic head for the caprock fracture to grow at a higher position (Fu et al. 2017).

669 Fig. 10(e) shows the cooling front in the reservoir rock has advanced a distance equal to

670 approximately half of the fracture height, nearly 40 m. This results in a significant decrease of

671 total stress perpendicular to the fracture, despite the poromechanical effect that tends to increase

672 the total stress (Fig. 10(n)). Meanwhile, the total stress of regions near the fracture front in the

673 caprock is not reduced by the thermo-mechanical effect but rather slightly increases (fig. 10(o)).

674 This stress increase is mostly owing to the additional compression of the caprock to compensate

675 for the cooling contraction of the reservoir. Other studies have also reported this compression of

676 the caprock induced by the injection of cold CO_2 into the reservoir (e.g. Vilarrasa and Laloui,

677 2015; Salimmda et al. 2017). In this state, the cooling of the reservoir tends to have opposite

678 effects on the total stresses of the reservoir and the caprock. Therefore, the net effect of this

679 discrepancy is that it is much easier to fracture the reservoir rock than the caprock.

680   Another key observation in this stage is a gradually decreasing injection pressure (Fig. 7(a)).

681   This pressure decrease is owing to the effect of cooling on the total stress of the fracture tip

682   region. In the second stage, the fracture tip region, located in the caprock, is largely unaffected

683   by the cooling front (Fig. 9(g)). In this stage, however, the cooling front has traversed the

684   fracture entirely and the near tip region has been cooled, which results in a decrease of total

685   stress (Fig. 10(h) and (p)) and therefore the fracturing pressure decreases.

686   Note that in all stages analyzed, the propagation of the fracture is still in the leak-off dominated

687   regime and the mass loss introduced by the coupling scheme is marginal, as clearly shown in

688   Fig.8(a). These results demonstrate that the proposed modeling scheme can be employed to

689   effectively simulate fracture propagation in a leakoff-dominated regime without compromising

690   its accuracy.

691   **5   Effects of the magnitude of *in situ* stresses in the caprock**

692   As reflected in the baseline simulation, the caprock *in situ* stress S_{Cap} plays significant roles in

693   determining the evolution of pumping pressure and affecting the pattern of fracture propagation.

694   However, to what extent the stress difference between S_{Cap} and S_{Rsv} affects the fracture

695   propagation and containment is still unclear. In this section, we evaluate the effects of S_{Cap} on the

696   growth and vertical containment of fluid-driven fractures. Note that $\bar{S}_{hmin}^{C}$ presented in this

697   section denotes the greatest horizontal minimum stresses in the caprock, which is the stress level

698   at the interface with the reservoir.

699   Fig. 11 shows the effects of $\bar{S}_{hmin}^{C}$ (varying from 26 MPa to 32 MPa) on fracture propagation and

700   fracture geometries (i.e. fracture heights and lengths). A lower $\bar{S}_{hmin}^{C}$ is expected to reduce

701   vertical containment of caprock fracturing. Especially in the case with $\bar{S}_{hmin}^{C}= 26$ MPa, the

702   maximum fracture height reaches around 192 m, far exceeding the thickness of the reservoir (i.e.,

703   24 m). However, the fracture heights (i.e., 32 and 40 m) in cases with $\bar{S}^C_{hmin}$= 30 and 32 MPa are

704   both slightly larger than 24 m and the fracture height (i.e., 88 m) in the baseline lies in between.

705   Meanwhile, the case with $\bar{S}^C_{hmin}$=26MPa where caprock fracturing leads the fracture growth

706   throughout the entire simulation has a long fracture length (i.e. 1053 m after 3 year of CO_2

707   injection (Fig. 11(a))), whereas the rest of the cases ($\bar{S}^C_{hmin}$=28MPa, 30MPa, and 32 MPa) have

708   shorter fracture lengths that are similar to each other (i.e. around 650 m at the end of the

709   simulation (Fig. 11(b), (c) and (d))). This discrepancy is caused by the significantly lower leakoff

710   coefficient for the case with $\bar{S}^C_{hmin}$=26MPa. First, the difference between the fracture pressure

711   and the pore pressure in the far field is lower in the case with $\bar{S}^C_{hmin}$=26 MPa compared with the

712   other cases for which pumping pressures are quite similar (Fig. 12(a)). This pressure difference

713   drives fluid leakoff from the fracture to the reservoir. Second, caprock fracturing leads the

714   fracturing process in the low caprock stress case such that the fracture only penetrates into the

715   reservoir a short distance, despite the larger overall height. In addition, the effective leakoff

716   contact area is only a small fraction of the entire height of the reservoir. The combination of

717   these factors determine that the low stress case has a lower leakoff coefficient and therefore a

718   longer fracture length.
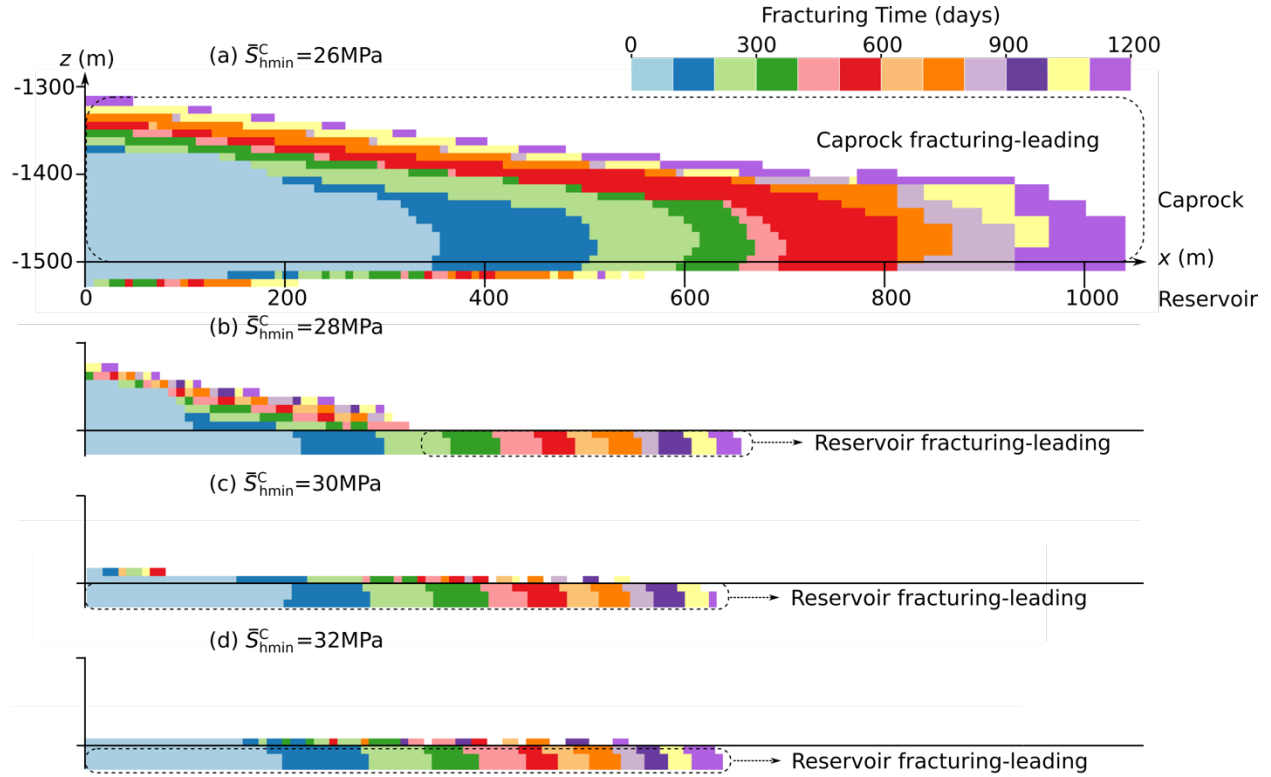
Fig. 11 Effect of the caprock *in situ* stress ((a) 26MPa, (b) 28MPa, (c) 30MPa, and (d) 32MPa) on the distribution of fracturing time along the fracture. Quantities are projected onto the the *x-z* plane.

The magnitude of $\bar{S}^C_{hmin}$ also greatly affects the evolution of injection pressure and maximum aperture (Fig. 12). When $\bar{S}^C_{hmin}$ is suffcently high to contain fracturing mostly within the reservoir ($\bar{S}^C_{hmin}$=28, 30, 32 MPa), the injection pressure, as disucssed in the previous section, experiences first a plateau and then a gradual decline. However, when caprock fracturing leads the overall fracturing throughout the injection ($\bar{S}^C_{hmin}$=26 MPa), the injection pressure remains largely constant after the fracture grows into the caprock.

Fig. 12(b) shows that maximum apertures in all cases experience continuous increases. Cooling induced by CO_2 injection in the near wellbore region tends to play convoluted roles in affecting maximum apertures under different $\bar{S}^C_{hmin}$ levels. For a caprock fracturing-leading case

732   ($\bar{S}^C_{hmin}$=26 MPa), the fracture-opening pressure, P^o_f, near the injection point, owing to the

733   thermal-mechanical effect, could drop significantly. However, the fracture propagation pressure,

734   P_p, which is dictated by the caprock *in situ* stress near the fracture front, remains largely

735   unchanged (Fig. 12(a)), thereby causing a high net pressure. This high net pressure, in

736   conjunction with the large overall fracture height, is likely to induce a large fracture aperture in

737   the near-wellbore region. As shown in Fig. 12(b), the maximum aperture in the case with

738    $\bar{S}^C_{hmin}$=26MPa reaches around 20 mm. Noticeably, this magnitude of maximum aperture far

739   exceeds the value predicted by isothermal fracture models (McClure and Horne, 2014; Fu et al.,

740   2017). Therefore, employing models that neglect the effects of thermo-elasticity for the

741   simulation of fracturing in GCS will tend to underestimate the magnitude of fracture apertures.

742   For a reservoir fracturing-leading case ($\bar{S}^C_{hmin}$=28, 30, 32 MPa), however, the fracture opening

743   pressure and the fracture propagation pressure both tend to decrease (Fig. 12(a)). In other words,

744   there might not be a monotonic increase of net pressure at this region as it is in the case with

745    $\bar{S}^C_{hmin}$=26 MPa, which explains a less remarkable increase of aperture magnitude. Meanwhile,

746   the maximum apertures for cases with $\bar{S}^C_{hmin}$=30MPa and 32MPa approach similar values after

747   300 days of injection. This means in the long run, provided the caprock stress is high enough to

748   prevent fracture propagation into the caprock, the exact magnitude does not play a significant

749   role in affecting the system response.
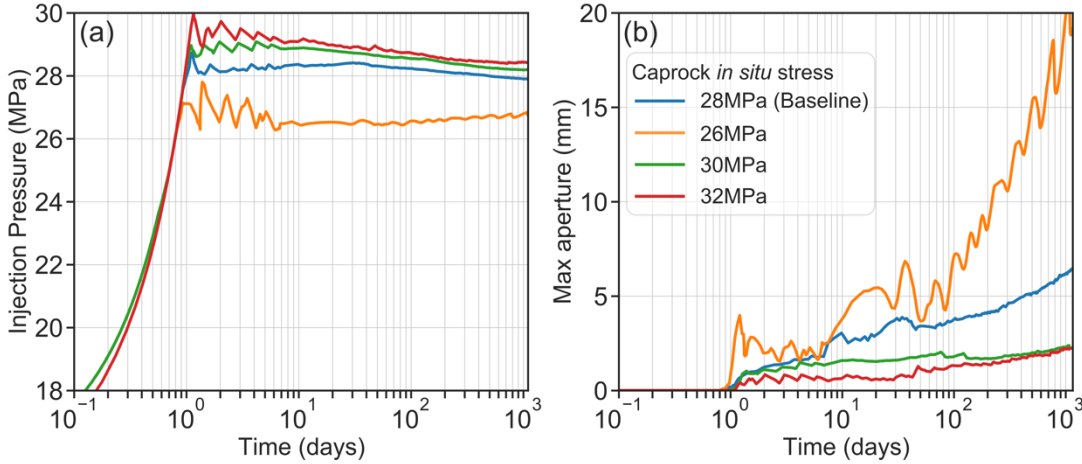
Fig. 12. Effect of the caprock *in situ* stress on (a) the injection pressure and (b) the maximum aperture. The apparent oscilation in the curves is caused by sudden pressure drop when the fracture propagates by the length of an element: a typical artifact for this type of space discretization scheme.

6   Concluding remarks

This paper develops an efficient and effective modeling scheme for simulating thermo-hydro-mechanical processes in fluid-driven fracturing. Such a modeling capability is crucial for studying geologic carbon storage (GCS) in reservoirs with marginal permeability where a hydraulic fracture could propagate in both the reservoir and caprock with complex phenomenology. The model captures multiphase multicomponent fluid flow and heat transfer within fractures and matrix, poro/thermo-mechanical deformation of solid rocks, and fracture propagation. Each of the physical processes is modeled using a robust individual module, and the modules are coupled utilizing a common simulation platform. In order to overcome the numerical challenges posed by coupling many complex processes, we take advantage of some self-stabilizing features of leakoff-dominated fracturing to simplify the numerical coupling. These features enable us to develop a sequential coupling scheme without convergence difficulties. Verification against the PKN solution in the leakoff-dominated regime indicates that

768   the simple scheme does not compromise the accuracy of the results for simulating leakoff-

769   dominated fracturing.

770   In simulating a 3D field-scale injection operation loosely based on the In Salah project, the

771   model reveals complex yet intriguing behaviors of the reservoir-caprock-fluid system. Soon after

772   the injection starts, back-stress caused by pressure diffusion in the reservoir drives a sharp

773   increase in injection pressure to keep the fracture open, until the pressure is high enough to drive

774   fracture propagation into the caprock. The injection pressure then remains largely constant at the

775   caprock's fracturing pressure. Injected fluid continued to be fed into the reservoir through the

776   slowly propagating fracture. Meanwhile, temperature decrease in the reservoir gradually reduces

777   the reservoir's total stress, and eventually the fracturing pressure of the reservoir becomes lower

778   than in the caprock. Thereafter the fracture mainly propagates in the reservoir, and the injection

779   pressure slowly declines accordingly. We also used the model to study the effects of the *in situ*

780   stress contrast between the reservoir and caprock on the vertical containment of the fracture.

781   We found many processes, including thermal, hydraulic, and mechanical processes, are involved

782   in fracturing caused by CO_2 injection. These processes have complex interactions and the

783   relative importance among these processes can evolve as injection progresses. The new model

784   proves effective in simulating these processes and their complex interactions in fidelity that is

785   unattainable for existing simple models. For example, thermal contraction induced by CO_2

786   injection has often been speculated to have a negative impact on fracture containment. Our study

787   shows that cold fluid injection itself could actually benefit the geomechanical containment of

788   fracturing under certain stress conditions within the caprock. Our results indicate that a gradual

789   pumping pressure decline can be used as a practical indicator of fracture growth during injection.

790   Despite the success in revealing the complex interactions among multiple physical processes, all

791   the simulations presented in this paper used simplified stress profiles. More realistic stress

792   profiles with layered fabric (Fisher and Warpinski, 2012) and "rough" in situ stress profiles (Fu

793   et al., 2019), should be considered to further assess the caprock integrity and system responses in

794   the future.

803   **Reference**

804   Bohloli, B., Ringrose, P., Grande, L., Nazarian, B., 2017. Determination of the fracture pressure

805   from CO_2 injection time-series datasets. Int. J. Greenh. Gas Control 61, 85–93.

806   https://doi.org/10.1016/j.ijggc.2017.03.025

807   Brooks, R.H., Corey, A.T., 1964. Hydraulic Properties of Porous Media. Hydrology Papers 3.

808   Colorado State University, Fort Collins, CO.

809   Bunger, A.P., Detournay, E., Garagash, D.I., 2005. Toughness-dominated hydraulic fracture with

810   leak-off. Int. J. Fract. 134, 175–190. https://doi.org/10.1007/s10704-005-0154-0

811   Eshiet, K.I.I., Sheng, Y., 2014. Carbon dioxide injection and associated hydraulic fracturing of

812   reservoir formations. Environ. Earth Sci. 72, 1011–1024. https://doi.org/10.1007/s12665-013-

813   3018-3

814   Carrier, B., Granet, S., 2012. Numerical modeling of hydraulic fracture problem in permeable

815   medium using cohesive zone model. Eng. Fract. Mech. 79, 312–328.

816   https://doi.org/10.1016/j.engfracmech.2011.11.012

817   Coussy, O., 2004. Poromechanics. John Wiley and Sons, Chichester, England.

818   Culp, D., Tupek, M.R., Newell, P., Hubler, M.H., 2017. Phase-field modeling of fracture in CO_2

819   sequestration. In: 51st US Rock Mechanics/Geomechanics Symposium. American Rock

820   Mechanics Association ARMA–2017–0644.

821   Detournay, E., Cheng, A.H.D., Roegiers, J.C., McLennan, J.D., 1989. Poroelasticity

822   considerations in In Situ stress determination by hydraulic fracturing. Int. J. Rock Mech. Min.

823   Sci. 26, 507–513. https://doi.org/10.1016/0148-9062(89)91428-9

824   Detournay, E., 2016. Mechanics of Hydraulic Fractures. Annu. Rev. Fluid Mech. 48, 311–339.

825   https://doi.org/10.1146/annurev-fluid-010814-014736

826   Dontsov, E. V., 2017. An approximate solution for a plane strain hydraulic fracture that accounts

827   for fracture toughness, fluid viscosity, and leak-off. Int. J. Fract. 205, 221–237.

828   https://doi.org/10.1007/s10704-017-0192-4

829   Fan, C., Elsworth, D., Li, S., Zhou, L., Yang, Z., Song, Y., 2019. Thermo-hydro-mechanical-

830   chemical couplings controlling CH4 production and CO_2 sequestration in enhanced coalbed

831   methane recovery. Energy 173, 1054–1077. https://doi.org/10.1016/j.energy.2019.02.126

832   Fu, P., Johnson, S.M., Carrigan, C.R., 2013. An explicitly coupled hydro-geomechanical model

833   for simulating hydraulic fracturing in arbitrary discrete fracture networks. Int. J. Numer. Anal.

834   Methods Geomech. 37, 2278–2300. https://doi.org/10.1002/nag.2135

835   Fu, P., Settgast, R.R., Hao, Y., Morris, J.P., Ryerson, F.J., 2017. The Influence of Hydraulic

836   Fracturing on Carbon Storage Performance. J. Geophys. Res. Solid Earth 122, 9931–9949.

837   https://doi.org/10.1002/2017JB014942

838   Fu, P., Huang, J., Settgast, R.R., Morris, J.P., Ryerson, F.J., 2019. Apparent toughness

839   anisotropy induced by "roughness" of in-situ stress: A mechanism that hinders vertical growth of

840   hydraulic fractures and its simplified modeling. SPE J. 24, 2148–2162.

841   https://doi.org/10.2118/194359-PA

842   Fu, P., Ju, X., Huang, J., Settgast, R. R., Morris, J. P., 2019. THM Modeling of Poroelastic

843   Sustainability of Hydraulic Fracture in CO_2 Storage Reservoirs. In American Rock Mechanics

844   Association. In *Proceedings of the 44th US Rock Mechanics Symposium,* New York, NY,

845   ARMA-2019-1601, 2019.

846   Fu, P., Ju, X., Huang, J., Settgast, R.R., Liu, F., Morris, J.P., 2020. Thermo-poroelastic responses

847   of a pressure-driven fracture in a carbon storage reservoir and the implications for injectivity and

848   caprock integrity. Int. J. Numer. Anal. Methods. Geomech. 1–19.

849   https://doi.org/10.1002/nag.3165

850   Francfort, G.A., Bourdin, B., Marigo, J.J., 2008. The variational approach to fracture, Journal of

851   Elasticity. https://doi.org/10.1007/s10659-007-9107-3

852   Francfort, G.A., Marigo, J.-J., 1998. Revisiting brittle fracture as an energy minimization

853   problem. J. Mech. Phys. Solids 46, 1319–1342. https://doi.org/10.1016/S0022-5096(98)00034-9

854   Fisher, K., Warpinski, N., 2012. Hydraulic-fracture-height growth: Real data. SPE Prod. Oper.

855   27, 8–19. https://doi.org/10.2118/145949-pa

856   Gheibi, S., Vilarrasa, V., Holt, R.M., 2018. Numerical analysis of mixed-mode rupture

857   propagation of faults in reservoir-caprock system in CO_2 storage. Int. J. Greenh. Gas Control 71,

858   46–61. https://doi.org/10.1016/j.ijggc.2018.01.004

859   Girault, V., Kumar, K., Wheeler, M.F., Wheeler, M.F., 2016. Convergence of iterative coupling

860   of geomechanics with flow in a fractured poroelastic medium. Comput. Geosci. 997–1011.

861   https://doi.org/10.1007/s10596-016-9573-4

862   Guo, B., Tao, Y., Bandilla, K., Celia, M., 2017. Vertically Integrated Dual-porosity and Dual-

863   permeability Models for CO_2 Sequestration in Fractured Geological Formation. Energy Procedia

864   114, 3343–3352. https://doi.org/10.1016/j.egypro.2017.03.1466

865   Gor, G.Y., Elliot, T.R., Prevost, J.H., 2013. Effects of thermal stresses on caprock integrity

866   during CO_2 storage. Int. J. Greenh. Gas Control 12, 300–309.

867   Haszeldine, R.S., 2009. Carbon Capture and Storage: How Green Can Black Be? Science. 325,

868   1647–1652. https://doi.org/10.1126/science.1172246

869   Huang, J., Fu, P., Settgast, R.R., Morris, J.P., Ryerson, F.J., 2019. Evaluating a Simple

870   Fracturing Criterion for a Hydraulic Fracture Crossing Stress and Stiffness Contrasts. Rock

871   Mech. Rock Eng. 52, 1657–1670. https://doi.org/10.1007/s00603-018-1679-7

872   Iding, M., Ringrose, P., 2010. Evaluating the impact of fractures on the performance of the In

873   Salah CO_2 storage site. Int. J. Greenh. Gas Control 4, 242–248.

874   https://doi.org/10.1016/j.ijggc.2009.10.016

875   International Energy Agency. Energy Technology Perspectives 2010: Scenarios and Strategies to

876   2050; 2010; International Energy Agency, Paris, France.

877   Ju, X., Liu, F., Fu, P., D. White, M., R. Settgast, R., P. Morris, J., 2020. Gas Production from

878   Hot Water Circulation through Hydraulic Fractures in Methane Hydrate-Bearing Sediments:

879   THC-Coupled Simulation of Production Mechanisms. Energy & Fuels 0.

880   https://doi.org/10.1021/acs.energyfuels.0c00241

881   Kim, J., Tchelepi, H.A., Juanes, R., 2011. Stability and convergence of sequential methods for

882   coupled flow and geomechanics: Fixed-stress and fixed-strain splits. Comput. Methods Appl.

883   Mech. Eng. 200, 1591–1606. https://doi.org/10.1016/j.cma.2010.12.022

884   Kim, J., Moridis, G., Yang, D., Rutqvist, J., 2012. Numerical Studies on Two-Way Coupled

885   Fluid Flow and Geomechanics in Hydrate Deposits. SPE J. 17, 485–501.

886   https://doi.org/10.2118/141304-PA

887   Kim, J., Moridis, G.J., 2013. Development of the T+M coupled flow-geomechanical simulator to

888   describe fracture propagation and coupled flow-thermal-geomechanical processes in tight/shale

889   gas systems. Comput. Geosci. 60, 184–198. https://doi.org/10.1016/j.cageo.2013.04.023

890   Kim, S., Hosseini, S.A., 2014. Geological CO_2 storage: Incorporation of pore-pressure/stress

891   coupling and thermal effects to determine maximum sustainable pressure limit. Energy Procedia

892   63, 3339–3346. https://doi.org/10.1016/j.egypro.2014.11.362

893   Kim, S., Hosseini, S.A., 2015. Hydro-thermo-mechanical analysis during injection of cold fluid

894   into a geologic formation. Int. J. Rock Mech. Min. Sci. 77, 220–236.

895   https://doi.org/10.1016/j.ijrmms.2015.04.010

896   Kovalyshen, Y. , 2010. Fluid-Driven Fracture in Poroelastic Medium. University of Minnesota.

897   Howard, G.C., Fast, C., 1957. Optimumfluid characteristics for fracture extension. Drill. Prod.

898   Prac. 24, 261–270.

899   Li, Z. and Elsworth, D., 2019. Controls of CO_2–N_2 gas flood ratios on enhanced shale gas

900   recovery and ultimate CO_2 sequestration. J. Pet. Sci. Eng. 179, 1037-1045.

901   Lecampion, B., Bunger, A., Zhang, X., 2018. Numerical methods for hydraulic fracture

902   propagation: A review of recent trends. J. Nat. Gas Sci. Eng. 49, 66–83.

903   https://doi.org/10.1016/j.jngse.2017.10.012

904   McClure, M.W., Horne, R.N., 2014. An investigation of stimulation mechanisms in Enhanced

905   Geothermal Systems. Int. J. Rock Mech. Min. Sci. 72, 242–260.

906   https://doi.org/10.1016/j.ijrmms.2014.07.011

907   Mito, S., Xue, Z., Ohsumi, T., 2008. Case study of geochemical reactions at the Nagaoka CO_2

908   injection site, Japan. Int. J. Greenhouse Gas Control 2, 309–318.

909   Moridis, G.J., Freeman, C.M., 2014. The RealGas and RealGasH2O options of the TOUGH+

910   code for the simulation of coupled fluid and heat flow in tight/shale gas systems. Comput.

911   Geosci. 65, 56–71. https://doi.org/10.1016/j.cageo.2013.09.010

912   Morris, J.P., Hao, Y., Foxall, W., McNab, W., 2011. A study of injection-induced mechanical

913   deformation at the In Salah CO_2 storage project. Int. J. Greenh. Gas Control 5, 270–280.

914   https://doi.org/10.1016/j.ijggc.2010.10.004

915   Mollaali, M., Ziaei-Rad, V., Shen, Y., 2019. Numerical modeling of CO_2 fracturing by the phase

916   field approach. J. Nat. Gas Sci. Eng. 70, 102905. https://doi.org/10.1016/j.jngse.2019.102905

917   Nordgren, R.P., 1972. Propagation of a Vertical Hydraulic Fracture. Soc. Pet. Eng. J. 12, 306–

918   314. https://doi.org/10.2118/3009-pa

919   Orr, F.M., 2009. Onshore geologic storage of CO_2. Science. 325, 1656–1658.

920   https://doi.org/10.1126/science.1175677

921   Oye, V., Aker, E., Daley, T.M., Kühn, D., Bohloli, B., Korneev, V., 2013. Microseismic

922   monitoring and interpretation of injection data from the In Salah CO_2 storage site (Krechba),

923   Algeria. Energy Procedia 37, 4191–4198. https://doi.org/10.1016/j.egypro.2013.06.321

924   Pacala, S., Socolow, R, 2004. Stabilization Wedges: Solving the Climate Problem for the Next

925   50 Years with Current Technologies. Science. 305, 968–972.

926   https://doi.org/10.1126/science.1100103

927 Paluszny, A., Graham, C.C., Daniels, K.A., Tsaparli, V., Xenias, D., Salimzadeh, S., Whitmarsh,

928 L., Harrington, J.F., Zimmerman, R.W., 2020. Caprock integrity and public perception studies of

929 carbon storage in depleted hydrocarbon reservoirs. Int. J. Greenh. Gas Control 98, 103057.

930 https://doi.org/10.1016/j.ijggc.2020.103057

931 Pan, L., Oldenburg, C.M., Pruess, K., Wu, Y.-S., 2011. Transient CO_2 leakage and injection in

932 wellbore-reservoir systems for geologic carbon sequestration. Greenh. Gases Sci. Technol. 1,

933 335–350. https://doi.org/10.1002/ghg.41

934 Perkins, T.K., Kern, L.R., 1961. Widths of Hydraulic Fractures. J. Pet. Technol. 13, 937–949.

935 https://doi.org/10.2118/89-pa

936 Raziperchikolaee, S., Alvarado, V., Yin, S., 2013. Effect of hydraulic fracturing on long-term

937 storage of CO_2 in stimulated saline aquifers. Appl. Energy 102, 1091–1104.

938 https://doi.org/10.1016/j.apenergy.2012.06.043

939 Ren, F., Ma, G., Wang, Y., Fan, L., Zhu, H., 2017. Two-phase flow pipe network method for

940 simulation of CO_2 sequestration in fractured saline aquifers. Int. J. Rock Mech. Min. Sci. 98, 39–

941 53. https://doi.org/10.1016/j.ijrmms.2017.07.010

942 Rinaldi, A.P., Rutqvist, J., 2013. Modeling of deep fracture zone opening and transient ground

943 surface uplift at KB-502 CO_2 injection well, In Salah, Algeria. Int. J. Greenh. Gas Control 12,

944 155–167. https://doi.org/10.1016/j.ijggc.2012.10.017

945   Ringrose, P.S., Mathieson, A.S., Wright, I.W., Selama, F., Hansen, O., Bissell, R., Saoula, N.,

946   Midgley, J., 2013. The in salah CO_2 storage project: Lessons learned and knowledge transfer.

947   Energy Procedia 37, 6226–6236. https://doi.org/10.1016/j.egypro.2013.06.551

948   Rutqvist, J., Vasco, D.W., Myer, L., 2010. Coupled reservoir-geomechanical analysis of CO_2

949   injection and ground deformations at In Salah, Algeria. Int. J. Greenh. Gas Control 4, 225–230.

950   https://doi.org/10.1016/j.ijggc.2009.10.017

951   Pruess, K., Tsang, Y.W., 1990. On two-phase relative permeability and capillary pressure of

952   rough-walled rock fractures. Water Resour. Res. 26, 1915–1926.

953   https://doi.org/10.1029/WR026i009p01915

954   Rutqvist, J., Rinaldi, A.P., Cappa, F., Moridis, G.J., 2013. Modeling of fault reactivation and

955   induced seismicity during hydraulic fracturing of shale-gas reservoirs. J. Pet. Sci. Eng. 107, 31–

956   44. https://doi.org/10.1016/j.petrol.2013.04.023

957   Salimzadeh, S., Paluszny, A., Zimmerman, R.W., 2017. Three-dimensional poroelastic effects

958   during hydraulic fracturing in permeable rocks. Int. J. Solids Struct. 108, 153–163.

959   https://doi.org/10.1016/j.ijsolstr.2016.12.008

960   Salimzadeh, S., Paluszny, A., Zimmerman, R.W., 2018. Effect of cold CO_2 injection on fracture

961   apertures and growth. Int. J. Greenh. Gas Control 74, 130–141.

962   https://doi.org/10.1016/j.ijggc.2018.04.013

963   Salimzadeh, S., Hagerup, E.D., Kadeethum, T., Nick, H.M., 2019. The effect of stress

964   distribution on the shape and direction of hydraulic fractures in layered media. Eng. Fract. Mech.

965   215, 151–163. https://doi.org/10.1016/j.engfracmech.2019.04.041

966   Senseny, P.E., Pfeifle, T.W., 1984. Fracture toughness of sandstones and shales. In: The 25th US

967   Symposium on Rock Mechanics (USRMS). 25–27 June, Evanston Illinois.

968   Settgast, R.R., Fu, P., Walsh, S.D.C., White, J.A., Annavarapu, C., Ryerson, F.J., 2016. A fully

969   coupled method for massively parallel simulation of hydraulically driven fractures in 3-

970   dimensions. Int. J. Numer. Anal. Methods Geomech. https://doi.org/10.1002/nag.2557

971   Sun, Z., Espinoza, D.N., Balhoff, M.T., 2016. Discrete element modeling of indentation tests to

972   investigate mechanisms of CO_2-related chemomechanical rock alteration. J. Geophys. Res. Solid

973   Earth 121, 7867–7881. https://doi.org/10.1002/2016JB013554

974   Sun, Z., Espinoza, D.N., Balhoff, M.T., Dewers, T.A., 2017. Discrete Element Modeling of

975   Micro-scratch Tests: Investigation of Mechanisms of CO_2 Alteration in Reservoir Rocks. Rock

976   Mech. Rock Eng. 50, 3337–3348. https://doi.org/10.1007/s00603-017-1306-z

977   Vilarrasa, V., Olivella, S., Carrera, J., Rutqvist, J., 2014. Long term impacts of cold CO_2

978   injection on the caprock integrity. Int. J. Greenh. Gas Control 24, 1–13.

979   https://doi.org/10.1016/j.ijggc.2014.02.016

980   Vilarrasa, V., Laloui, L., 2015. Potential fracture propagation into the caprock induced by cold

981   CO_2 injection in normal faulting stress regimes. Geomech. Energy Environ. 2, 22–31.

982   Vilarrasa, V., Rinaldi, A.P., Rutqvist, J., 2017. Long-term thermal effects on injectivity evolution

983   during CO_2 storage. Int. J. Greenh. Gas Control 64, 314–322. DOI: 10.1016/j.ijggc.2017.07.019

984   White, J.A., Chiaramonte, L., Ezzedine, S., Foxall, W., Hao, Y., Ramirez, A., McNab, W., 2014.

985   Geomechanical behavior of the reservoir and caprock system at the In Salah CO_2 storage project.

986   Proc. Natl. Acad. Sci. 111, 8747–8752. https://doi.org/10.1073/pnas.1316465111

987   White, J.A., Castelletto, N., Tchelepi, H.A., 2016. Block-partitioned solvers for coupled

988   poromechanics: A unified framework. Comput. Methods Appl. Mech. Eng. 303, 55–74.

989   https://doi.org/10.1016/j.cma.2016.01.008

990   Witherspoon, P.A., Wang, J.S.Y., Iwai, K., Gale, J.E., 1980. Validity of Cubic Law for fluid

991   flow in a deformable rock fracture. Water Resour. Res. 16, 1016–1024.

992   https://doi.org/10.1029/WR016i006p01016

993   Yan, H., Zhang, J., Zhou, N., Li, M., Suo, Y., 2020. Numerical simulation of dynamic

994   interactions between two cracks originating from adjacent boreholes in the opposite directions

995   during supercritical CO_2 fracturing coal mass. Eng. Fract. Mech. 223, 106745.

996   https://doi.org/10.1016/j.engfracmech.2019.106745

997   Van Genuchten, M.T., 1980. A closed-form equation for predicting the hydraulic conductivity of

998   unsaturated soils. Soil Sci. Soc. Am. J. 44 (5), 892–898.